REPORT DOCUMENTATION PAGE

Form Approved
OMB No. 0704-0188

PLEASE DO NOT RETURN YOUR FORM TO THE ABOVE ORGANIZATION.

1. REPORT DATE *(DD-MM-YYYY)*	2. REPORT TYPE	3. DATES COVERED *(From - To)*
04-01-2007	Final Technical Report	01-01-2005 - 12-31-2006

4. TITLE AND SUBTITLE
Calibration and Compensation Of Instrumental Errors in Imaging Polarimeters

5a. CONTRACT NUMBER

5b. GRANT NUMBER
FA9550-05-1-0090

5c. PROGRAM ELEMENT NUMBER

6. AUTHOR(S)
J. Scott Tyo and Majeed M. Hayat

5d. PROJECT NUMBER

5e. TASK NUMBER

5f. WORK UNIT NUMBER

7. PERFORMING ORGANIZATION NAME(S) AND ADDRESS(ES)
University of New Mexico
Scholes Hall
Albuquerque, NM 87131

8. PERFORMING ORGANIZATION REPORT NUMBER

9. SPONSORING/MONITORING AGENCY NAME(S) AND ADDRESS(ES)
AFOSR/NE
4015 Wilson BLVD, Room 713
Arlington, VA 22203

10. SPONSOR/MONITOR'S ACRONYM(S)

11. SPONSOR/MONITOR'S REPORT NUMBER(S)

12. DISTRIBUTION/AVAILABILITY STATEMENT
Unlimited
Distribution Statement A: unlimited

AFRL-SR-AR-TR-07-0125

13. SUPPLEMENTARY NOTES

14. ABSTRACT
The measurement and exploitation of polarization information has become a high priority in a variety of Air Force and DoD remote sensing missions. Polarization provides a useful dimension of information that helps to characterize shape and surface characteristics of interesting targets in optical imagery from the UV through the LWIR and beyond. There are a number of ongoing efforts that are developing specific instruments to quantitatively measure polarization information across a scene. We have discovered that polarization is important, but it can also be quite difficult to measure accurately. Optical systems designed to respond to polarization information are usually more complex than those that respond to spectral information. In addition, most polarimeters require linear combinations of multiple looks at a single pixel in order to infer the polarization parameters. In contrast, most spectral imagers (certain Fourier transform devices excepted) can form the spectrum at a pixel in a single integration time without comparing measurements from different sensors.

15. SUBJECT TERMS
Remote Sensing, Polarization, IR Imaging

16. SECURITY CLASSIFICATION OF:			17. LIMITATION OF ABSTRACT	18. NUMBER OF PAGES	19a. NAME OF RESPONSIBLE PERSON
a. REPORT	b. ABSTRACT	c. THIS PAGE			J. Scott Tyo
U	U	U	U		19b. TELEPHONE NUMBER *(Include area code)* 520-626-8183

Final Technical Report

Calibration and Compensation Of Instrumental Errors in Imaging Polarimeters

Award Number: FA9550-05-1-0090
January 1, 2005 – December 31, 2006

Submitted to:
Dr. Kent Miller
AFOSR/NE
4015 Wilson BLVD, Room 713
Arlington, VA 22203

PI: J. Scott Tyo
Electrical and Computer Engineering Department
University of New Mexico
Albuquerque, NM 87131-1356 USA
tyo@ieee.org

co-PI: Majeed M. Hayat
Electrical and Computer Engineering Department
University of New Mexico
Albuquerque, NM 87131-1356 USA
hayat@ece.unm.edu

ABSTRACT

The measurement and exploitation of polarization information has become a high priority in a variety of Air Force and DoD remote sensing missions. Polarization provides a useful dimension of information that helps to characterize shape and surface characteristics of interesting targets in optical imagery from the UV through the LWIR and beyond. There are a number of ongoing efforts that are developing specific instruments to quantitatively measure polarization information across a scene. We have discovered that polarization is important, but it can also be quite difficult to measure accurately. Optical systems designed to respond to polarization information are usually more complex than those that respond to spectral information. In addition, most polarimeters require linear combinations of multiple looks at a single pixel in order to infer the polarization parameters. In contrast, most spectral imagers (certain Fourier transform devices excepted) can form the spectrum at a pixel in a single integration time without comparing measurements from different sensors. Because polarization imagers are more complex, uncalibrated instrumental errors can be even more damaging to the quality of the final imagery. This research project was focused on understanding the instrumental effects on imaging polarimeters and compensating for them in the final imagery.

1. OBJECTIVES

The original objectives of this research program were:

1. Identify useful error metrics for polarization imagery.
2. Develop rigorous calibration procedures for polarimeters
3. Examine impact of focal plane nonuniformity on polarimeters
4. Understand the role of bandwidth in broadband polarimetry.
5. Upgrade the Polarimeter Testbed in the MDIL

2. MAJOR ACCOMPLISHMENTS & FINDINGS

2.1. Development of a Polarimeter Model to Use in Calibration and Verification

Polarimetry in the LWIR is complicated by the presence of emitted radiation from the scene background as well as the instrument. This complication results in all measured signatured actually being a combination of two signatures. The first is the emitted signature of the target of interest, which is what we are after. The second is the reflected signature of the target and background illuminant. Demixing these two signals is complicated in real data.

To address this issue, we initially developed a end-to-end polarimeter model that allowed us to understand how the polarized radiometric signatures propagated through the instrument. The instrument model begins at the scene, producing a thermal Stokes image from a defined temperature, emissivity, and geometry image. That is then propagated through the imaging optics of the system to provide the Stokes vector incident on the individual pixels. At this point, we use calibration information to convert the incident radiance into electronic units (counts, current, etc.)

The value of the end-to-end model is that it allows us to study the effects of particular physical phenomena, calibration errors, etc. We used the model successfully to refine our calibration routines for use with the real polarimeters that we operated.

More details on the end-to-end model can be found in the archived publication.

- J. K. Boger, M. P. Fetrow, J. S. Tyo, R. Kumar, B. M. Ratliff, "Modeling precision and accuracy of an LWIR microgrid array imaging polarimeter," *Proc SPIE Vol. 5888: Polarization Science and Remote Sensing II*, pp. 58880U 1 – 10, J. A. Shaw and J. S. Tyo, Eds., (SPIE, Bellingham, 2005)

2.2. Impact of NU Noise on Polarimeters

Infrared (IR) polarimetry presents a set of unique challenges that are not seen in other areas of the optical spectrum. Some of these challenges include the presence of both reflected and emitted radiation with polarization signatures that cancel,[1] low signal-to-noise ratios, and expensive detectors and optics. In addition, a particular problem associated with IR focal plane arrays (FPAs) is nonuniformity (NU) noise. NU noise is a results from pixel-to-pixel variations in the photodetector response.

NU noise is a persistent problem for all LWIR imagers. For LWIR polarimeters, NU noise presents a special problem because it impacts the component measurements that go into estimating the Stokes vector. The class of polarimeters known as microgrid polarimeters[2,3] as especially susceptible to NU noise because of the local spatial differencing that must occur.

We performed a simulation study of the effects of NU noise on the performance of all classes of LWIR polarimeters. We found that conventional NUC techniques can be helpful with polarimeters, but must be augmented by fully polarimetry NUC for best results. Full details of these studies can be obtained in the following publications.

- B. M. Ratliff, R. Kumar, J. S. Tyo, and M. M. Hayat, "Combatting infrared focal plane array nonuniformity noise in imaging polarimeters," *Proc SPIE Vol. 5888: Polarization Science and Remote Sensing II*, pp. 58880J 1 – 10, J. A. Shaw and J. S. Tyo, Eds., (SPIE, Bellingham, 2005)
- B. M. Ratliff, J. S. Tyo, J. K. Boger, W. T. Black, D. M. Bowers, and M. P. Fetrow "Dead pixel replacement in LWIR microgrid polarimeters," submitted to to *Opt. Exp.*, April 2007 (manuscript included as appendix A)

2.3. Correction of IFOV errors in Microgrid Polarimeters

The microgrid polarimeter that we considered is designed to work in the long-wave infrared (LWIR) 7.8 - 9.8 μm band and has a mosaic of wire-grid polarizers placed on a HgCdTe focal plane array (FPA). In this scheme, each polarization measurement is acquired spatially and hence each is made at a different point in the scene. This is a significant source of error, as it violates the requirement that each polarization measurement have the same instantaneous field-of-view (IFOV).

There are a number of potential methods to combat this issue. One common approac is an optical method that designs the point spread function to overlap with a superpixel, thereby mitigating IFOV error. However, this strategy also eliminates high-spatial-frequency information from the scene, reducing the top resolution possible with the system. We have focused on image processing methods to combat IFOV errors. These methods use spatial image information (usually from the s_0 channel) to improve our estimates of the locally changing scene. We have had significant results that show great improvement using hybrid interpolation techniques. Our methods and results are presented in the following publication.

- Bradley M. Ratliff, James K. Boger, Matthew P. Fetrow, J. Scott Tyo, and Wiley T. Black, "Image processing methods to compensate for IFOV errors in microgrid imaging polarimeters," *Proc. SPIE 6240*, 62400E (2006)

2.4. Radiometric Calibration of LWIR Microgrid Polarimeter

The unpolarized, or radiometric, calbration of the polarimeter allows the conversion of the direct output of the pixels on the FPA to the radiometric units that we need to compute the Stokes vector. Ideally the component radiances would be taken at a single pixel that is aligned. However, the microgrid method forces the component radiances to be measured at offset positions. This offset is instantaneous field-of-view (IFOV) error, and many techniques have been explored to mitigate it.[3,4] Because of the small polarization signals and the spatial differencing, polarization products including DoLP are more sensitive to NUC than is thermal imagery. Consequently, the DoLP is used as a primary metric for gauging the camera polarimetric sensitivity.

We have extensively studied the impact of radiometric calibration of the polarimeter on the final polarization products. We began by separating the calibration process into two parts: an unpolarized calibration and a polarized calibration. We were able to completely decouple these, allowing the two calibrations to be completely independent. In the arena of radiometric calibration, we have carefully studied the false polarization signatures associated with different calibration routines, including one-point, two-point, and multi-point calibrations. We find significant false polarization (5%) even for unpolarized scenes, especially when the scene temperatures are outside the calibration temperatures. We found that the polarization products are *significantly* more sensitive to calibration than the corresponding s_0 image.

For details of these studies, please see the following publications.

- David L. Bowers, James K. Boger, L. David Wellems, Wiley T. Black, Steve E. Ortega, Bradley M. Ratliff, Matthew P. Fetrow, John E. Hubbs, and J. Scott Tyo, "Evaluation and display of polarimetric image data using long-wave cooled microgrid focal plane arrays," *Proc. SPIE 6240*, 62400F (2006)
- David L. Bowers, James K. Boger, L. David Wellems, Wiley T. Black, Steve E. Ortega, Bradley M. Ratliff, Matthew P. Fetrow, John E. Hubbs and J. Scott Tyo, "Unpolarized Calibration and Nonuniformity Correction for LWIR Microgrid Imaging Polarimeters," submitted to *Opt. Eng.* April 2007 (manuscript included as Appendix B)

2.5. Polarimetric Calibration of LWIR Microgrid Polarimeters

We extended the radiometric calibration work described in the previous section to include a fully polarimetric calibration of the microgrid system on a pixel-by-pixel basis. Obtaining a calibrated **DRM** is the goal of this work. We then went on to describe two methods by which the needed calibration coefficients are estimated. This is done because we have found that the measured calibration coefficients are not exact and that the polarimetric calibration will be limited by the accuracy of these data. In the simplest description, one method requires a greater level of effort and was assumed to be a better estimate. Polarimetric calibration is hoped to improve the polarimetric accuracy and improve the final image product. We concluded by carefully examining the impacts of calibration on data. This is done in several different ways since no one

metric is sufficient in gauging the multiple benefits of polarimetric calibration. The final metric is to gauge the impact of applying the calibrated **DRM** to an actual polarimetric image.

Details of this study can be found in the following publication.

- James K. Boger, David L. Bowers, Wiley T. Black, Steve E. Ortega, Bradley M. Ratliff, Matthew P. Fetrow, John E. Hubbs and J. Scott Tyo, "The Role of Calibration in the Performance of LWIR Microgrid Polarimeters: Polarized Calibration," In preparation for submission to *Opt. Eng.* (Manuscript included as appendix C)

2.6. Effects of Thermal Equilibrium on LWIR Polarimetry

Polarimetric imagers are usually designed to sense the polarization properties of the reflected polarization signatures, though it is well known that emitted radiation can also be partially polarized.[5] In order to have enough emitted radiation to reliably detect the polarization signatures, it is been necessary to either work with very hot targets or sense in the long-wave infrared (LWIR, $8 - 12\ \mu$m). There has been interest in LWIR imaging polarimetry dating back more than 20 years,[6] with many imaging and non-imaging devices built and tested in the intervening years.[2] The purported advantages of polarimetric sensing in the LWIR include independence from any external source of radiation and invariance of signatures with respect to time-of-day. These advantages are assumed to come from the fact that the source of radiation is thermal emission from objects in the scene.

In our research, we found that LWIR polarimetry is significantly complicated by the presence of emitting backgrounds. We presented striking experimental evidence of the complete elimination of polarization signatures when an object is in themral equilibrium with its background. This was the first such dynamic demonstration in the LWIR. For details of this study, see the following publiction.

- J. S. Tyo, J. K. Boger, B. M. Ratliff, D. Bowers, W. T. Black, and M. P. Fetrow, "The Effects of Thermal Equilibrium and Thermal Contrast in Polarimetric Images in the LWIR," In preparation for submission to *Applied Optics* (Manuscript included as Appendix D)

2.7. Upgrade of the MDIL Facilty at UNM

There has been significant recent interest in the optimization of polarimeter systems, especially those designed for the remote sensing of polarization imagery. These studies have been motivated by a desire to improve the signal-to-noise-ratio (SNR) and the performance of the polarimeter in the presence of systematic calibration errors. These studies have been largely theoretical, and have not presented much experimental evidence of the theoretical predictions. In this portion of the effort, we studied the design of an automated polarization characterization system that we use to test the theoretical hypothesis about the optimization of polarimeters. We obtained results for rotating retarder polarimeters, and verified that quarter waveplates are not the optimum retarders to use in the presence of error and noise. Our results agreed with predictions, but we find that the relative balance between noise and error is delicate.

For details of this study, please see the following publication.

- H. Wei and J. S. Tyo, "Automated polarization characterization system," *Proc SPIE Vol. 5888: Polarization Science and Remote Sensing II*, pp. 58881M 1 – 10, J. A. Shaw and J. S. Tyo, Eds., (SPIE, Bellingham, 2005)

3. PERSONNEL SUPPORTED

The following individuals at UNM were supported by this award:

1. J. Scott Tyo, Associate Professor, ECE Department
2. Majeed M. Hayat, Associate Professor, ECE Department
3. James K. Boger, Research Associate, ECE Department
4. Rakesh Kumar, PhD Student, ECE Department

5. Hue Wei, PhD Student, ECE Department

The following individuals at UNM were associated with the project but not supported:

1. Wiley Black, Undergraduate Student, ECE Department
2. Sara Stratton, Undergraduate Student, ECE Department

The following Individuals at AFRL were associated with this project but not supported by the funds:

1. Matthew P. Fetrow, Group Leader, AFRL/VSSS
2. David Bowers, Engineer, Applied Technology Associates
3. David Wellems, Physicist, Applied Technology Associates

4. PUBLICATIONS

4.1. Peer Reviewed (or in peer review)

1. J. S. Tyo, "Hybrid Division of Aperture/Division of Focal Plane Polarimeter for Real-Time Polarization Imagery without IFOV Error," *Opt. Lett* **31**:2984 – 2986 (2006)
2. J. S. Tyo and H. Wei, "Imaging Polarimetry with Imperfect Optics," *Applied Opt.*, **45**:5497 – 5503 (2006)
3. J. S. Tyo, D. H. Goldstein, D. B.Chenault, and J. A. Shaw, "A Review of Passive Imaging Polarimetery for Remote Sensing Applications," *Applied Opt.*, **45**:5453–5469 (2006)
4. B. M. Ratliff, J. S. Tyo, J. K. Boger, W. T. Black, D. M. Bowers, and M. P. Fetrow "Dead pixel replacement in LWIR microgrid polarimeters," submitted to to *Opt. Exp.*, April 2007 (manuscript included as appendix A)
5. David L. Bowers, James K. Boger, L. David Wellems, Wiley T. Black, Steve E. Ortega, Bradley M. Ratliff, Matthew P. Fetrow, John E. Hubbs and J. Scott Tyo, "Unpolarized Calibration and Nonuniformity Correction for LWIR Microgrid Imaging Polarimeters," submitted to *Opt. Eng.* April 2007 (manuscript included as Appendix B)
6. James K. Boger, David L. Bowers, Wiley T. Black, Steve E. Ortega, Bradley M. Ratliff, Matthew P. Fetrow, John E. Hubbs and J. Scott Tyo, "The Role of Calibration in the Performance of LWIR Microgrid Polarimeters: Polarized Calibration," In preparation for submission to *Opt. Eng.* (Manuscript included as appendix C)
7. J. S. Tyo, J. K. Boger, B. M. Ratliff, D. Bowers, W. T. Black, and M. P. Fetrow, "The Effects of Thermal Equilibrium and Thermal Contrast in Polarimetric Images in the LWIR," In preparation for submission to *Applied Optics* (Manuscript included as Appendix D)

4.2. Edited Conference Proceedings Papers

1. B. M. Ratliff, R. Kumar, J. S. Tyo, and M. M. Hayat, "Combatting infrared focal plane array nonuniformity noise in imaging polarimeters," *Proc SPIE Vol. 5888: Polarization Science and Remote Sensing II*, pp. 58880J 1 – 10, J. A. Shaw and J. S. Tyo, Eds., (SPIE, Bellingham, 2005)
2. H. Wei and J. S. Tyo, "Automated polarization characterization system," *Proc SPIE Vol. 5888: Polarization Science and Remote Sensing II*, pp. 58881M 1 – 10, J. A. Shaw and J. S. Tyo, Eds., (SPIE, Bellingham, 2005)
3. J. K. Boger, M. P. Fetrow, J. S. Tyo, R. Kumar, B. M. Ratliff, "Modeling precision and accuracy of an LWIR microgrid array imaging polarimeter," *Proc SPIE Vol. 5888: Polarization Science and Remote Sensing II*, pp. 58880U 1 – 10, J. A. Shaw and J. S. Tyo, Eds., (SPIE, Bellingham, 2005)
4. David L. Bowers, James K. Boger, L. David Wellems, Wiley T. Black, Steve E. Ortega, Bradley M. Ratliff, Matthew P. Fetrow, John E. Hubbs, and J. Scott Tyo, "Evaluation and display of polarimetric image data using long-wave cooled microgrid focal plane arrays," *Proc. SPIE 6240*, 62400F (2006)
5. Bradley M. Ratliff, James K. Boger, Matthew P. Fetrow, J. Scott Tyo, and Wiley T. Black, "Image processing methods to compensate for IFOV errors in microgrid imaging polarimeters," *Proc. SPIE 6240*, 62400E (2006)

5. INTERACTIONS

5.1. Conference Participation

The following conferences were participated in by members of the research team relevant to this research award:

1. SPIE Defense and Security Symposium, Orlando FL, March 2005
2. SPIE Polarization Science and Remote Sensing II, San Diego, CA August 2005.
3. CALCON 2005, Space Dynamics Lab, Utah State University, August 2005
4. SPIE Defense and Security Symposium, Orlando FL, April 2006
5. 2006 OSA Annual Meeting, Rochester, NY, October 2007

5.2. Consultative and Advisory Functions

The PI was an external reviewer in 2005 for NA-22 for a project at Sandia National Labs called "Deimos." Deimos is a remote sensing technology incubator program, and includes a polarization research component.

5.3. Transitions

The work described in this report is in direct support of mission-related activities at AFRL/VSSS. The research team was intimately involved in the calibration and testing of a new IR polarization camera manufactured by DRS Sensors for AFRL. The model and laboratory measurement presented here transitioned directly into the fielded camera system that was used in the summer of 2005 for field tests. AFRL POC; Matthew P. Fetrow, AFRL/VSSS, 3550 Aberdeen SE, kirtland AFB, NM, 87117, 505-853-3523.

6. NEW DISCOVERIES, INVENTIONS, OR PATENT DISCLOSURES

None

7. HONORS/AWARDS

No honors or awards were received by project participants in the period of performance.

REFERENCES

1. J. A. Shaw, "Degree of linear polarization in spectral radiances from water-viewing infrared polarimeters," *Appl. Opt.* **38**, pp. 3157–3165, 1999.
2. J. S. Tyo, D. H. Goldstein, D. B. Chenault, and J. A. Shaw, "Review of passive imaging polarimetry for remote sensing applications," *Appl. Opt.* **45**, pp. 5453 – 5469, August 2006.
3. A. G. Andreou and Z. K. Kalayjian, "Polarization imaging: principles and integrated polarimeters," *IEEE Sensors Journal* **2**, pp. 566 – 576, 2002.
4. B. M. Ratliff, J. K. Boger, M. P. Fetrow, J. S. Tyo, and W. T. Black, "Image processing methods to compensate for ifov errors in microgrid imaging polarimeters," in *Proc. SPIE vol. 6240: Polarization: Measurement, Analysis, and Remote Sensing VII*, D. H. Goldstein and D. B. Chenault, eds., p. 6240OE, SPIE, Bellingham, WA, 2006.
5. O. Sandus, "A review of emission polarization," *Appl. Opt.* **4**, pp. 1634–1642, 1965.
6. T. J. Rogne, "Passive detection using polarized components of infrared signatures," in *Proceedings of SPIE vol. 1317: Polarimetry: Radar, infrared visible, ultraviolet and X-ray*, R. A. Chipman and J. W. Morris, eds., pp. 242 – 251, SPIE, (Bellingham, WA), 1990.

Dead Pixel Replacement in LWIR Microgrid Polarimeters

Bradley M. Ratliff
Applied Technology Associates, 1300 Britt St. SE, Albuquerque, NM 87123 USA

J. Scott Tyo
College of Optical Sciences, University of Arizona, Tucson, AZ 85721 USA
tyo@ieee.org

James K. Boger+, Wiley T. Black, David L. Bowers
Applied Technology Associates, 1300 Britt St. SE, Albuquerque, NM 87123 USA

Matthew P. Fetrow
US Air Force Research Laboratory/VSSS, 3550 Aberdeen SE, Kirtland AFB, NM 87117 USA

Abstract: LWIR imaging arrays are often affected by nonresponsive pixels, or "dead pixels." These dead pixels can severely degrade the quality of imagery and often have to be replaced before subsequent image processing and display of the imagery data. For LWIR arrays that are integrated with arrays of micropolarizers, the problem of dead pixels is amplified. Conventional dead pixel replacement (DPR) strategies cannot be employed since neighboring pixels are of different polarizations. In this paper we present two DPR schemes. The first is a modified nearest-neighbor replacement method. The second is a method based on redundancy in the polarization measurements. We find that the redundancy-based DPR scheme provides an order-of-magnitude better performance for typical LWIR polarimetric data.

OCIS codes: (000.0000) General.

References and links

1. R. A. Millikan, "A study of the polarization of the light emitted by incandescnet solid and liquid surfaces. I." Phys. Rev. **3**, 81–99 (1895).
2. R. A. Millikan, "A study of the polarization of the light emitted by incandescnet solid and liquid surfaces. II." Phys. Rev. **3**, 177–192 (1895).
3. O. Sandus, "A review of emission polarization," Appl. Opt. **4**, 1634–1642 (1965).
4. T. J. Rogne, "Passive detection using polarized components of infrared signatures," in *Proceedings of SPIE vol. 1317: Polarimetry: Radar, infrared visible, ultraviolet and X-ray*, R. A. Chipman and J. W. Morris, eds., pp. 242 – 251 (SPIE, Bellingham, WA, 1990).
5. J. S. Tyo, D. H. Goldstein, D. B. Chenault, and J. A. Shaw, "Review of Passive Imaging Polarimetry for Remote Sensing Applications," Appl. Opt. **45**, 5453 – 5469 (2006). and references therein.
6. A. G. Andreou and Z. K. Kalayjian, "Polarization imaging: principles and integrated polarimeters," IEEE Sensors Journal **2**, 566 – 576 (2002).
7. D. L. Perry and E. L. Dereniak, "Linear theory of nonuniformity correction in infrared staring sensors," Opt. Eng. **32**, 1854–1859 (1993).
8. R. Walraven, "Polarization Imagery," Opt. Eng. **20**, 14 – 18 (1981).
9. J. S. Tyo, "Optimum Linear Combination Strategy For A N-Channel Polarization Sensitive Vision Or Imaging System," J. Opt. Soc. Am. A **15**, 359–366 (1998).
10. J. S. Tyo, "Design of optimal polarimers: maximization of SNR and minimization of systematic errors," Appl. Opt. **41**, 619–630 (2002).

11. D. S. Sabatke, M. R. Descour, E. Dereniak, W. C. Sweatt, S. A. Kemme, and G. S. Phipps, "Optimization of Retardance for a Complete Stokes Polarimeter," Opt. Lett. **25**, 802–804 (2000).
12. B. M. Ratliff, J. K. Boger, M. P. Fetrow, J. S. Tyo, and W. T. Black, "Image processing methods to compensate for IFOV errors in microgrid imaging polarimeters," in *Proc. SPIE vol. 6240: Polarization: Measurement, Analysis, and Remote Sensing VII*, D. H. Goldstein and D. B. Chenault, eds., p. 6240OE (SPIE, Bellingham, WA, 2006).
13. J. K. Boger, J. S. Tyo, B. M. Ratliff, M. P. Fetrow, W. Black, and R. Kumar, "Modeling precision and acuracy of a LWIR microgrid array imaging polarimeter," in *Proc. SPIE vol. 5888: Polarization Science and Remote Sensing II*, J. A. Shaw and J. S. Tyo, eds. (SPIE, Bellingham, WA, 2005). In Press.
14. D. Bowers, J. K. Boger, L. D. Wellens, W. T. Black, S. E. Ortega, B. M. Ratliff, M. P. Fetrow, J. E. Hubbs, and J. S. Tyo, "Evaluation and display of polarimetric image data using long-wave cooled microgrid focal plane arrays," in *Proc. SPIE vol. 6240: Polarization: Measurement, Analysis, and Remote Sensing VII*, D. H. Goldstein and D. B. Chenault, eds., p. 6240OF (SPIE, Bellingham, WA, 2006).
15. L. B. Wolff, "Polarization Camera For Computer Vision With A Beam Splitter," J. Opt. Soc. Am. A **11**, 2935–2945 (1994).
16. G. P. Nordin, J. T. Meier, P. C. Deguzman, and M. . Jones, "Diffractive optical element for Stokes vector measurement with a focal plane array," in *Proceedings of SPIE vol. 3754, Polarization Measurement, Analysis, and Remote Sensing II*, D. H. Goldstein and D. B. Chenault, eds., pp. 169–177 (SPIE, Bellingham, WA, 1999).

1. Introduction

Imaging polarimetry in the long-wave infrared (LWIR, $8 - 12\ \mu$m) has been developed as a remote sensing method that can help to detect and identify objects of interest that may not have significant thermal contrast. The LWIR is an especially interesting part of the optical spectrum because the source of the detected radiation is usually emission from the object that is being imaged. The emissive nature of the optical signature makes LWIR images largely independent of external environmental parameters such as illumination an view angle.

The general problem of emissive polarimetry dates back more than a century [1, 2]. It is well known that emitted radiation can be polarized upon refraction out of the material through Fresnel transmission [3]. LWIR imaging polarimetry has been studied for almost as long as LWIR cameras have been available [4]. Numerous systems have been built that demonstrate the ability of LWIR polarimetry to aid in applications ranging from object detection and identification to imaging in scattering media [5].

Recent advances in the technology of LWIR sensing have enabled the development of integrated linear polarimeters that combine a LWIR focal plane array (FPA) with an array of wire grid micropolarizers in order to produce a division of focal plane (DoFP) polarimeter as depiceted in fig. 1. DoFP devices have been used in all regions of the optical spectrum and have been made with many different combinations of polarization patterns [6]. Importantly, these devices are usually mechanically rugged, inherently aligned optomechanically, and temporally synchronized, making them ideal for deployment

Focal plane array (FPA) sensors all suffer from the common problem of unresponsive pixels. These pixels are often termed "dead pixels" and affect the quality of both the visual image and the underlying data. Dead pixels are those pixels whose measurement does not have any correlation with the true scene that is being measured. They severely degrade the quality of measured imagery and require that their measurements be replaced with more appropriate values to improve image quality to an acceptable level that depends on the subsequent processing and display that the image is subjected to. Dead pixels impact the performance of all FPA sensors, but are especially problematic in the LWIR regime. Though the problem of dead pixel replacement (DPR) is well understood for existing FPA imagery [7], these techniques do not directly apply to imagery obtained from microgrid polarimeters because neighboring pixels are masked with different polarization filters.

Polarization imagery estimated from microgrid arrays is particularly sensitive to dead pixels, largely due to the spatial differencing that is required to obtain the polarization estimates. Standard FPA DPR techniques, such as nearest-neighbor, mean or median value replacement[7],

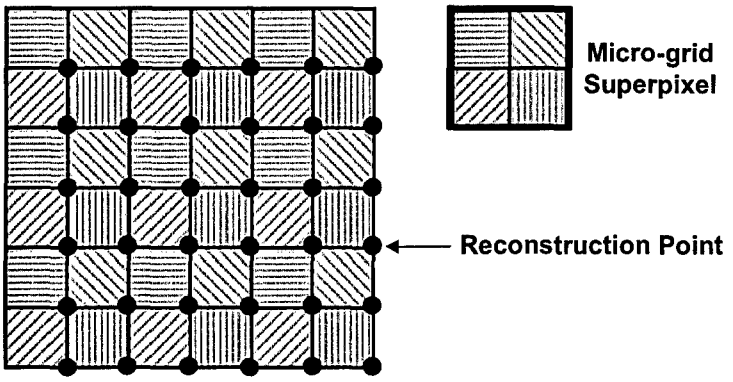

Fig. 1. Layout of the microgrid FPA depicting the 2×2 superpixels that contain all four micro-polarizer orientations.

cannot be directly applied to microgrid imagery due to the modulated polarizer measurements; a dead pixel within a microgrid-acquired image cannot be reliably replaced with a pixel from a different polarizer orientation. This complication requires that alternative schemes be developed to properly handle DPR for microgrid instruments. Such microgrid DPR strategies are presented in this paper. In particular, we present two techniques: 1) a modified nearest-neighbor approach; and 2) a microgrid-unique approach that relies on the inherent redundancy in the polarization measurements to estimate the missing intensity values.

It is important to note that determination of whether a pixel is dead or not is a significant topic in and of itself. The criteria for making such a determination can be defined in many ways and is not discussed here. For the purposes of dead pixel replacement, we assume that we have a binary image of the same dimensions as the focal plane image such that a dead pixel is indicated with a "1" and a properly functioning pixel is indicated by a "0". This binary image is called the dead pixel map and it is assumed that this map already exists in all replacement strategy discussions below.

The remainder of this paper is organized as follows. Section 2 discusses a DPR method based on nearest-neighbor replacement. Section 3 presents a more advanced method that allows dead pixels to be replaced by exploiting redundancy. Section 4 discusses and compares the performance of these two methods. Conclusions are presented in section 5.

2. Nearest Like-polarization Neighbor Replacement Scheme

One of the fastest and simplest DPR schemes that is commonly used on standard FPA imagery is nearest neighbor replacement. In this scheme a dead pixel's value is simply replaced with the value of one of its neighboring pixels. The only condition is that the replacing pixel not be a dead pixel itself. This method cannot be directly applied to the microgrid sensor because, for a given pixel, all of its adjacent neighbors contain measurements that were obtained through different polarization filters as shown in fig. 1. We must therefore put the additional constraint that the dead pixel's value only be replaced with the value of a pixel with the same polarization. This so-called nearest like-polarization neighbor (NLPN) replacement is visualized in Fig. 2. Notice that only pixels of the same polarizer orientation as the dead pixel are colored blue. The darker blue pixels are the best candidates for replacement because they are the closest to the dead pixel. In the case that the nearest pixels are themselves dead, we would then continue examining pixels of like polarization until we find the closest pixel of like polarization that is

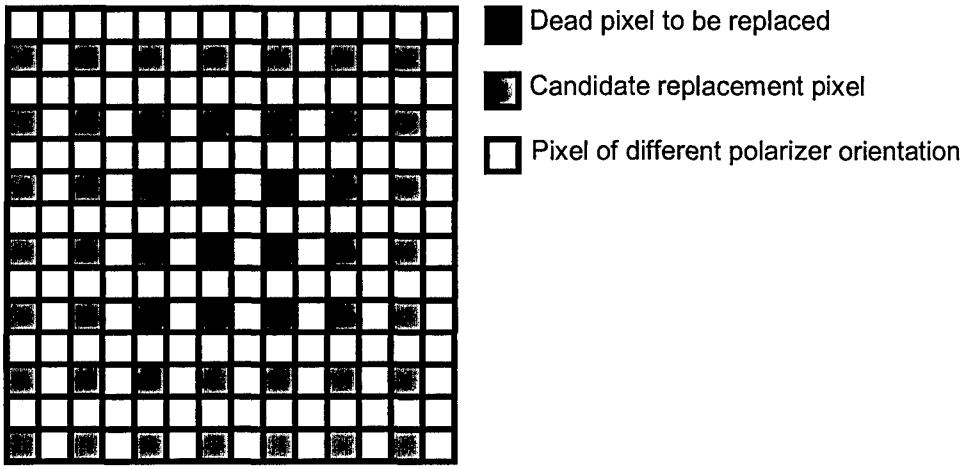

Fig. 2. Candidate pixels used for replacement of a dead pixel in the nearest like-polarization neighbor (NLPN) replacement scheme. The darker blue pixels are chosen first because they have the closest Euclidean distance to the dead pixel. The algorithm will select pixels farther away only when the closest ones are themselves dead.

not dead itself.

The NLPN method has similar advantages and disadvantages to nearest-neighbor methods for conventional, non-polarized arrays. The NLPN scheme is advantageous in that it is very fast from an implementation standpoint. One reason for this is that the closest not-dead-like-polarization pixel to be used for replacement can be determined *a priori*. Thus, a given dead pixel map can be algorithmically analyzed and all replacement pixels determined. This only has to be done once so that fewer computations are needed at run-time. In our implementation we replace each "1" in the dead pixel map with the relative offset from the dead pixel to the index of the replacement pixel. It is also worth noting that images can be represented as 1D arrays and we thus compute only a 1D offset. This is also useful in that we can represent each replacement pixel with a single number, rather than keeping track of two separate index offsets. Again, these relative offsets are computed *apriori* so that these computations do not have to be made at run-time, is a clear advantage of the NLPN technique.

The scheme can be disadvantageous in regions were there are large clusters of dead pixels, resulting in poor replacements due to the scheme having to replace these pixels with values that are far away. When the image is relatively flat in intensity content, NLPN replacement will still work well, but when there are large intensity gradients in the scene dead pixel clusters tend to persist in the imagery due to the significant deviation in the replacement value. An obvious disadvantage of the NLPN method compared with nearest-neighbor techniques for conventional FPAs is that the replacement pixel is always at least $\sqrt{2}$ pixels away from the dead pixel.

In addition to arbitrary choice of the NLPN, it is possible to implement a replacement that average over like polarization neighbors or randomly select among equal-distant like polarization neighbors. These alterations impact the performance of the DPR method in predictable ways using linear systems analysis.

3. Redundancy Estimation Replacement Scheme

Another DPR approach that yields performance superior to the NLPN technique is a scheme that we call redundancy estimation (RE). Estimation of the three linear Stokes parameters requires that three appropriate intensity measurements be made. In the case of the microgrid depicted in fig. 1 we have four intensity measurements (at 0° 45° 90° and 135°). It is common to use four linear polarization measurements to estimate the linear Stokes parameters [8], and the additional measurement – if chosen optimally [9] – can enhance the robustness of the polarization estimate [10, 11]. Furthermore, four measurements fit conveniently with the rectangular layout of our FPA.

Because of our four linear polarization measurements, we have one more measurement than is required to estimate the Stokes vector. This inherent redundancy in microgrid imagery can be exploited to our advantage. We do this by realizing that a given intensity measurement can be estimated from three of its neighboring pixels, each of a different polarizer orientation.

3.1. Determinating Redundancy

The device that we are working with only measures the linear polarization parameters. We define the reduced dimensionality Stokes vector as

$$\hat{\mathbf{S}} = \begin{bmatrix} \hat{s}_0 \\ \hat{s}_1 \\ \hat{s}_2 \end{bmatrix} = \begin{bmatrix} \frac{1}{2}(\hat{I}_0 + \hat{I}_{90} + \hat{I}_{45} + \hat{I}_{135}) \\ \hat{I}_{90} - \hat{I}_0 \\ \hat{I}_{135} - \hat{I}_{45} \end{bmatrix} \tag{1}$$

where $\hat{I}_x$ is the intensity estimated for a polarizer oriented in direction x at the specific spatial location where the Stokes vector is being estimated. The estimation scheme can be one of many that have been designed to mitigate IFOV errors [12], and the choice of interpolation method is not discussed here.

For the purposes of this discussion, we will assume that the micropolarizers are ideal. This means that their extinction ratios are much greater than 1. With this assumption, we can write the intensity measured by the pixels as

$$\begin{aligned} \hat{I}_0 &= \tfrac{1}{2}(\hat{s}_0 + \hat{s}_1); \quad \hat{I}_{45} = \tfrac{1}{2}(\hat{s}_0 + \hat{s}_2) \\ \hat{I}_{90} &= \tfrac{1}{2}(\hat{s}_0 - \hat{s}_1); \quad \hat{I}_{135} = \tfrac{1}{2}(\hat{s}_0 - \hat{s}_2) \end{aligned} \tag{2}$$

Using the four above relationships we find that we can solve for $\hat{s}_0$, $\hat{s}_1$ and $\hat{s}_2$ in multiple ways to yield the following set of equations:

$$\begin{array}{lll} \hat{s}_0 = \hat{I}_0 + \hat{I}_{90}; & \hat{s}_0 = \hat{I}_{45} + \hat{I}_{135} & \\ \hat{s}_1 = \hat{I}_0 - \hat{I}_{90}; & \hat{s}_1 = 2\hat{I}_0 - \hat{I}_{45} - \hat{I}_{135}; & \hat{s}_1 = \hat{I}_{45} - 2\hat{I}_{90} + \hat{I}_{135} \\ \hat{s}_2 = \hat{I}_{45} - \hat{I}_{135}; & \hat{s}_2 = 2\hat{I}_{45} - \hat{I}_0 - \hat{I}_{90}; & \hat{s}_2 = \hat{I}_0 - 2\hat{I}_{45} + \hat{I}_{90} \end{array} \tag{3}$$

Thus, there are two ways to compute s_0 and three ways to compute both s_1 and s_2. Notice in each case that all four intensity measurements are not used. Rearranging these equations we find that each intensity term can be expressed in terms of the intensities of the three other orientations such that

$$\begin{aligned} \bar{I}_0 &= \hat{I}_{45} - \hat{I}_{90} + \hat{I}_{135}; \quad \bar{I}_{45} = \hat{I}_0 + \hat{I}_{90} - \hat{I}_{135} \\ \bar{I}_{90} &= -\hat{I}_0 + \hat{I}_{45} + \hat{I}_{135}; \quad \bar{I}_{135} = \hat{I}_0 - \hat{I}_{45} + \hat{I}_{90} \end{aligned} \tag{4}$$

With the above relationships we now have a means for estimating a given pixel's value from three of its neighbors of differing orientation. The utility of this for DPR is clear.

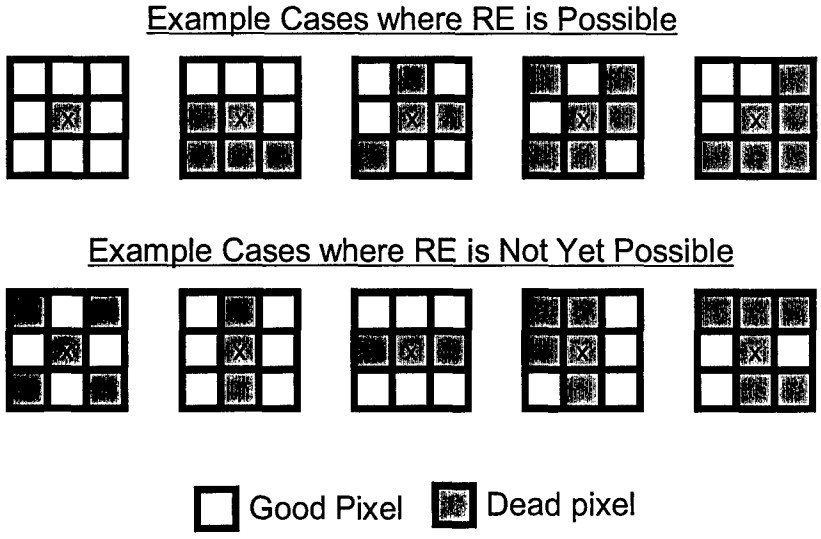

Fig. 3. Example cases illustrating when RE can/cannot estimate the value of a given dead pixel (indicated with an "x"). The requirement is that there be at least one good neighboring pixel from each of the three polarizer orientations opposite the dead pixel's.

3.2. DPR Implementation

To begin the development of a DPR replacement algorithm using the above redundancy relationships, we first discuss the case of a dead pixel where all of its neighboring pixels are not-dead. The first observation to make is that a given pixel always has neighbors that consist of four pixels of one orientation, two pixels of another orientation with the final two being of yet another orientation, as shown in fig. 1. The polarizer orientation of all of these pixels are different from the orientation of the dead pixel itself. When all of these neighbors are not-dead we first average each group of pixels of like orientation. Then, we simply use these averaged pixel values with the appropriate case in Eq. (4) to estimate the dead pixel's value. In the case when some of the neighboring pixels are dead themselves we must first analyze the neighbors to determine if there is at least one pixel from each of the three required orientations. If this is true, then we average all pixels of like orientation that are not dead and estimate the missing value. When pixels from the three orientations are not available we cannot yet estimate the dead pixel's value, but will be able to later once neighboring dead pixels are replaced. Thus, this DPR scheme may require that multiple passes be made to estimate all dead pixel values. Fig. 3 demonstrates some example cases that show when estimation is both possible and not possible when neighboring dead pixels are present.

When there are dead pixels that cannot be replaced on a given iteration of the algorithm we must continually reapply the algorithm until all dead pixels are replaced. In order to guarantee that this happens we must keep track of which pixels are replaced during a given iteration and then update the current dead pixel map at the end of the pass. Updating the dead pixel map at the end of the current iteration (rather than at the time when the dead pixel is replaced) will cause the algorithm to replace dead pixels in a particular order. For example, say that there is a cluster of dead pixels that is 3×3 in size and the algorithm iterates in a row/column fashion beginning at the top-left corner of the image. If the dead pixel map is updated at the time when replacement occurs then this entire cluster would be replaced in a single iteration. While this

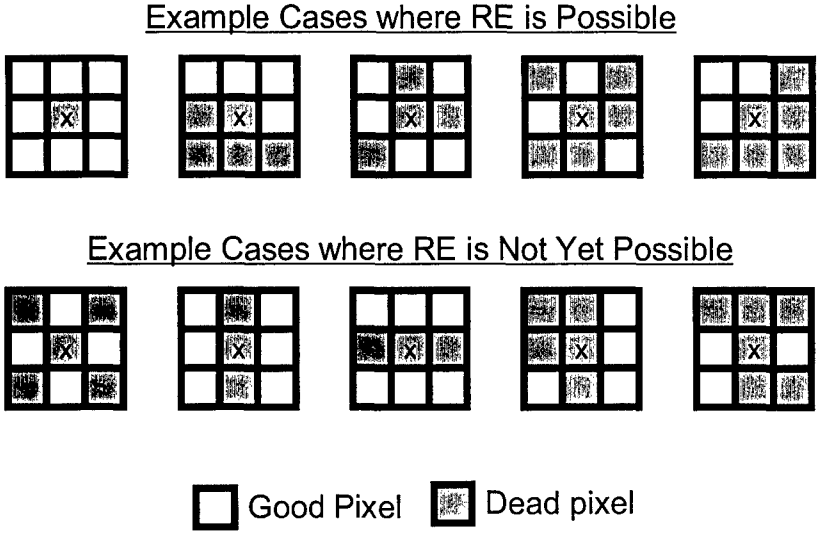

Fig. 3. Example cases illustrating when RE can/cannot estimate the value of a given dead pixel (indicated with an "x"). The requirement is that there be at least one good neighboring pixel from each of the three polarizer orientations opposite the dead pixel's.

3.2. DPR Implementation

To begin the development of a DPR replacement algorithm using the above redundancy relationships, we first discuss the case of a dead pixel where all of its neighboring pixels are not-dead. The first observation to make is that a given pixel always has neighbors that consist of four pixels of one orientation, two pixels of another orientation with the final two being of yet another orientation, as shown in fig. 1. The polarizer orientation of all of these pixels are different from the orientation of the dead pixel itself. When all of these neighbors are not-dead we first average each group of pixels of like orientation. Then, we simply use these averaged pixel values with the appropriate case in Eq. (4) to estimate the dead pixel's value. In the case when some of the neighboring pixels are dead themselves we must first analyze the neighbors to determine if there is at least one pixel from each of the three required orientations. If this is true, then we average all pixels of like orientation that are not dead and estimate the missing value. When pixels from the three orientations are not available we cannot yet estimate the dead pixel's value, but will be able to later once neighboring dead pixels are replaced. Thus, this DPR scheme may require that multiple passes be made to estimate all dead pixel values. Fig. 3 demonstrates some example cases that show when estimation is both possible and not possible when neighboring dead pixels are present.

When there are dead pixels that cannot be replaced on a given iteration of the algorithm we must continually reapply the algorithm until all dead pixels are replaced. In order to guarantee that this happens we must keep track of which pixels are replaced during a given iteration and then update the current dead pixel map at the end of the pass. Updating the dead pixel map at the end of the current iteration (rather than at the time when the dead pixel is replaced) will cause the algorithm to replace dead pixels in a particular order. For example, say that there is a cluster of dead pixels that is 3×3 in size and the algorithm iterates in a row/column fashion beginning at the top-left corner of the image. If the dead pixel map is updated at the time when replacement occurs then this entire cluster would be replaced in a single iteration. While this

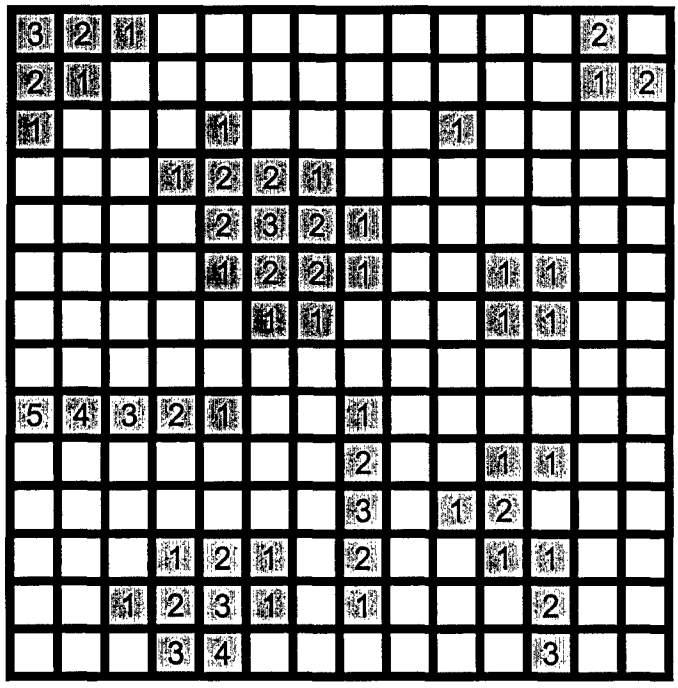

Fig. 4. Sample dead pixel patterns and the iteration that the dead pixel is replaced under the RE DPR scheme.

is desirable computationally it tends to be less accurate for replacement because it causes the replacement values to be biased with information from pixels above and to the left of the dead pixel cluster. If the dead pixel map is updated at the end of the iteration, this cluster would instead require three iterations to correct. In the first iteration only the four corner pixels would be corrected. The second iteration would then estimate the four other outer pixels and the third would then estimate the center pixel. This approach is more desirable in that it works in an outside/inward way that incorporates values from all pixels surrounding the cluster and yields better results in the replacement. Figure 4 shows some sample dead pixel patterns and the iteration on which each pixel is replaced using this latter update rule.

The RE strategy is advantageous in that it results in highly accurate estimates of the missing dead pixel values and is particularly superior to the NLPN technique. Its disadvantage is that it requires that the estimates be computed at run-time and therefore is not as computationally efficient as the NLPN technique. Though we don't discuss the details here, there are a number of computations that can be made *a priori* to reduce the number of decisions that must be made at run-time, such as which iteration a pixel will be updated on and what not-dead neighbors it should use in the computation.

4. Discussion

4.1. DPR Scheme Comparison

In this section we apply both the NLPN and RE techniques to real microgrid data and compare their performance. Each technique is demonstrated on the multi-point calibrated image of Fig. 5.b. This image was acquired with a LWIR microgrid polarimeter. The FPA was manu-

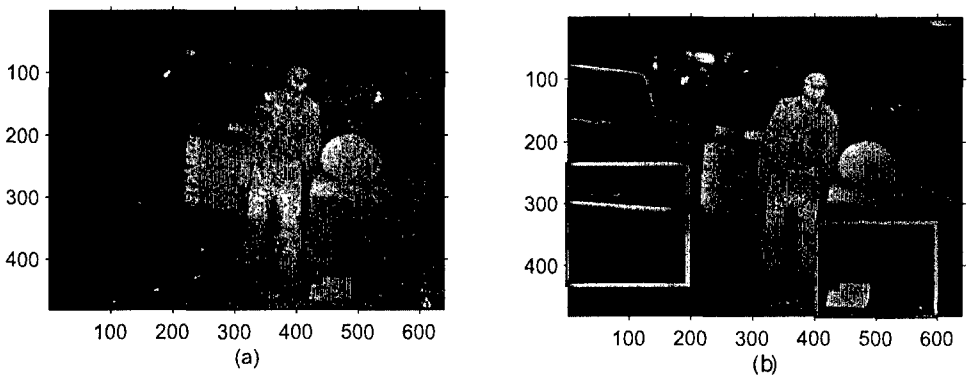

Fig. 5. Test images: (a) raw uncalibrated microgrid image; (b) image after multi-point calibration but before dead pixel replacement. The red-outlined regions are sub-images that are investigated in greater detail below.

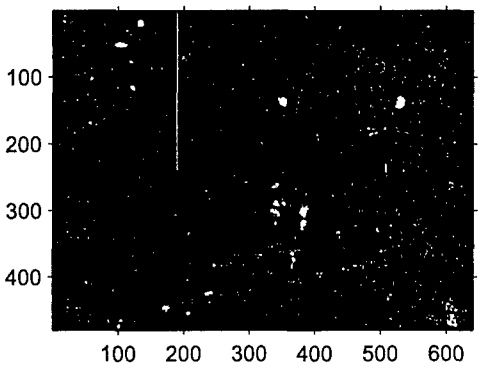

Fig. 6. Dead pixel map for the sensor.

factured by DRS Sensors and Tracking Systems, and operated in the 8 – 10 μm range. Details of the development, calibration, and operation of the sensor are presented elsewhere [13, 14]. We have a dead pixel map associated with this sensor obtained from the calibration procedure as shown in Fig. 6. Notice that in addition to there being a significant number of dead pixels throughout the image that there are several large clusters of dead pixels as well as a column where nearly half of the pixels are dead. For this sensor 2.9% of the pixels are flagged as being dead.

To better observe the dead pixels after calibration Fig. 7 shows two regions of this image as indicated by the boxes in fig. 5. In each region there are a significant number of dead pixels that are observed. Figure 8 shows the images that result from applying the NLPN and RE techniques to the image of Fig. 5.b. In both images notice that the results appear quite similar at first glance. To better see the resulting images Fig. 9 shows the same regions as Fig. 7 for each DPR technique. Once again, the resulting images from each technique appear quite similar, though in the NLPN-applied image we see that there are some values near edges that are not well-replaced. In particular, there are still dead pixels that can be observed near the truck grill and bumper at regions where there is strong thermal contrast in Fig. 9.a and near the edges of

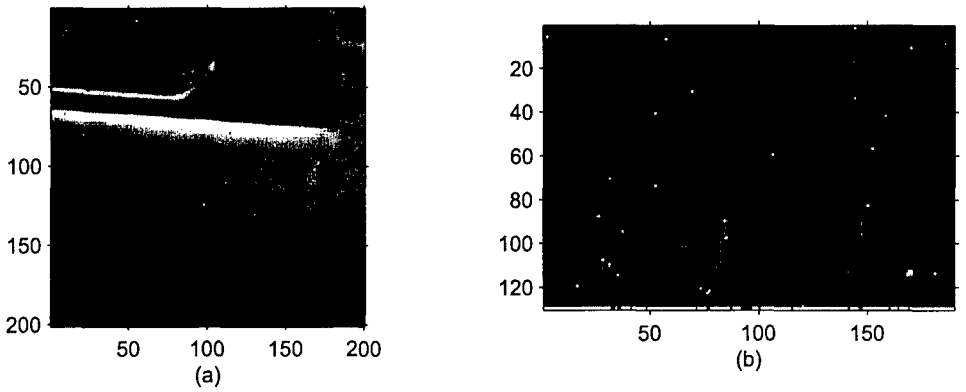

Fig. 7. Regions of the multi-point calibrated image of Fig. 5.b: (a) Image region (1 200) × (230 430) and (b) image region (401 590) × (351 480).

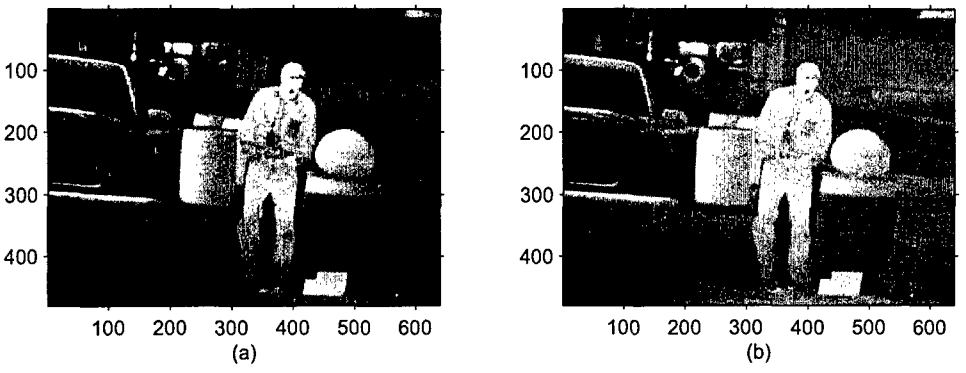

Fig. 8. The multi-point calibrated image of Fig. 5.b after application of the (a) NLPN and (b) RE replacement schemes.

the positioned plates in Fig. 9.c. In the RE-applied image there are no remaining dead pixels that are noticeable.

In order to quantify the performance of the two methods, we performed a simulation experiment. Starting with the calibrated image in fig. 5, we randomly eliminated 5.8% of the good pixels, resulting in a total of 8.7% dead pixels in the image. For all pixels that were *not dead*, we can then compare the estimated intensity to the original intensity. Histograms of the performance of the two methods are presented in fig. 10, and statistical data is tabulated in table 1.

Table 1. Statistics of the normalized error of the DPR schemes.

method	**mean**	**St. Dev.**
NLPN	-0.005%	3.6%
RE	-0.002%	0.43%

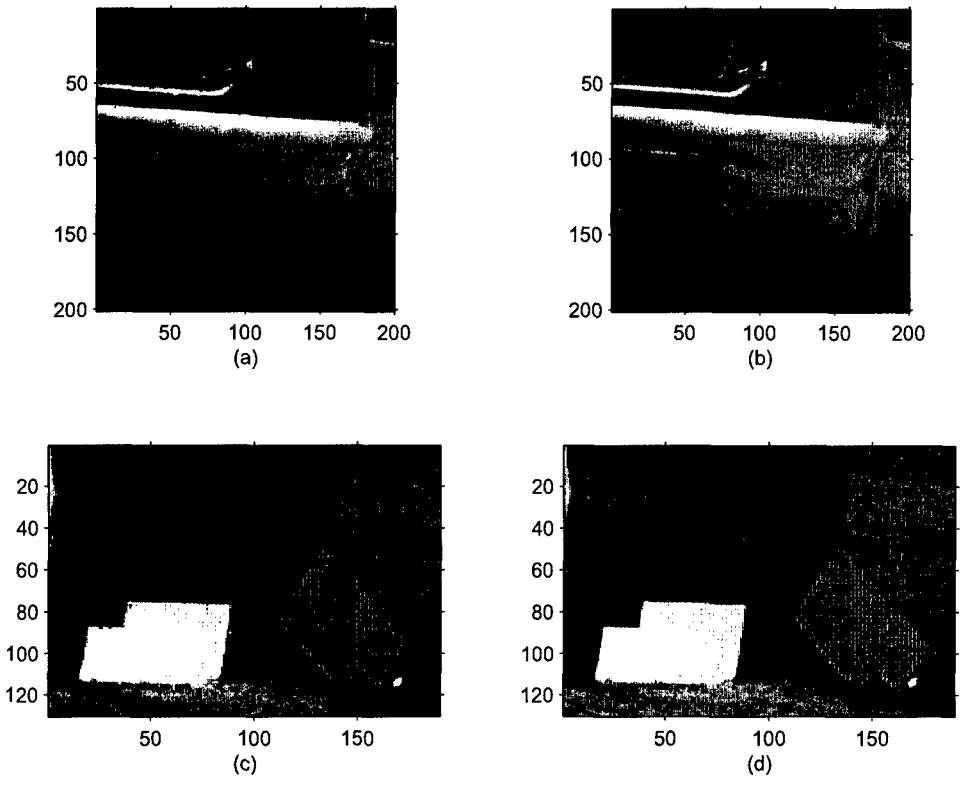

Fig. 9. Zoomed regions of the NLPN and RE corrected images of Fig. 8: (a) NLPN and (b) RE image region (1 200) × (230 430); (c) NLPN and (d) RE image region (401 590) × (351 480).

We see from fig. 10 and table 1 that both DPR methods produce unbiased estimators of the actual missing measured intensity. However, the RE scheme results in almost an order of magnitude improvement in performance over the NLPN method. It should be noted that these results are for a particular measured image. However, this image is diverse, containing both low- and high spatial frequency variations throughout the scene.

4.2. Impact on Polarimetric Images

While both techniques perform well at replacing the dead pixels in the raw multi-point calibrated image, poorly replaced dead pixels can reemerge in the polarization images. This is due to the polarization images being more sensitive to incorrect values because of the differencing that is required in their estimation. To see this the DoLP images are computed for each of the zoomed regions of Fig. 9 and displayed in Fig. 11. In each NLPN-DoLP image notice that many of the dead pixels are clearly visible whereas in the RE-DoLP image the dead pixels are not. We find that in general the RE DPR scheme yields better replacement values for dead pixels than the NLPN technique at the cost of being slightly more computational expensive. The RE technique should thus always be employed when possible with the NLPN technique being reserved for cases when computational speed is paramount.

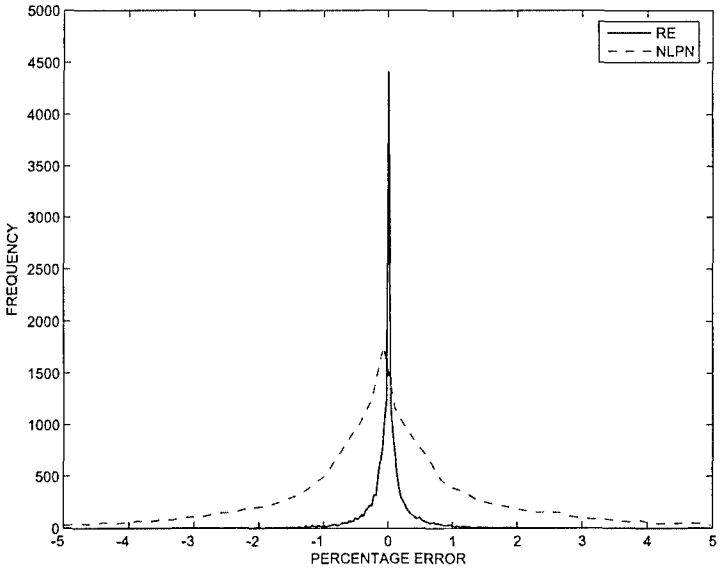

Fig. 10. Histogram of the relative error of the replaced pixels using the two methods discussed in this paper. The relative error was computed by replacing *good* pixels with the values predicted using the NLPN and RE schemes, then comparing to the actual value at that pixel.

4.3. Alternate interpretations

It is important to note that the DPR schemes presented above can not add information to the image that was lost due to the dead pixel in question. The methods that we have presented can be thought of as ways of minimizing the impact of the dead pixels on the polarization products that are computed from the raw data. Consider the case of a superpixel that has three good pixels and one dead pixel. Without loss of generality, we assume that the dead pixel is horizontally polarized. If we compute $\hat{s}_1$ at the center of this super pixel using our replaced value of I_0, we have

$$\hat{s}_1 = \bar{I}_0 - \hat{I}_{90} \quad (5)$$

$$= \hat{I}_{45} + \hat{I}_{135} - 2\hat{I}_{90} \quad (6)$$

$$= \hat{s}_0 - 2\hat{I}_{90} \quad (7)$$

where we have estimated s_0 in (7) using only $\hat{I}_{45}$ and $\hat{I}_{135}$. This is the standard method for computing the Stokes vector from a sub-optimal selection of linear three polarization states, and is widely used [15, 9].

We see then that our DPR scheme is functionally equivlent to identifying the dead pixels and then changing the computation method for estimating the Stokes vector in the vicinity of the dead pixels. We prefer the present implementation for the following reasons. First of all, it is numerically more efficient to use the same mathematical operator to compute the Stokes vector at every pixel in the scene. Use of a pixel-by-pixel variation would require more memory and more complicated processing algorithms. Second, it is often advantageous to use more advanced interpolation schemes that compensate for IFOV error in computing the Stokes vector[12]. The multi-pass processing scheme allows the choice of the interpolation method to be changed

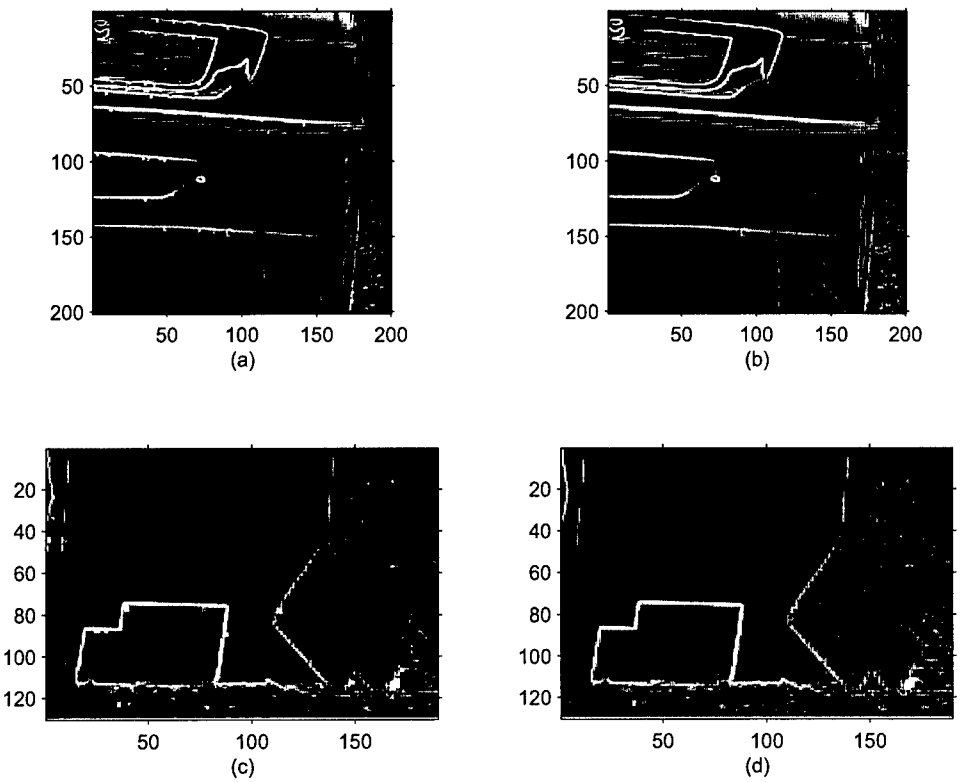

Fig. 11. Zoomed regions of the DoLP images computed using the no-interpolation method from the NLPN and RE corrected images of Fig. 8: (a) NLPN and (b) RE DoLP image region $(1\ 200) \times (230\ 430)$; (c) NLPN and (d) RE DoLP image region $(401\ 590) \times (351\ 480)$.

quickly wihtout impacting other features of the image processing system. These considerations are important when generating real-time polarimetric products from the microgrid polarimeter.

5. Conclusion

The problem of dead pixels affects all LWIR imagers, and is a difficult problem in the calibration of these devices. The dead pixel represents a fundamental loss of information that cannot be recovered. DPR methods have been developed for LWIR thermal imagers that make assumptions about the spatial variation within the scene, and a nearest-neighbor replacement method is widely used for conventional imagery. When the LWIR imager is integrated with a microgrid polarizer array to form a DoFP polarimeter, the problem of dead pixels is exacerbated. The assumptions about the similarity of neighboring pixels are now affected by the fact that the closest neighbors are operating at a different polarization state as indicated in fig. 1.

In this paper we discuss two possible DPR methods that recognize the difficulties associated with the DoFP imager strategy. The NLPN scheme replaces a dead pixel with the value at the nearest non-dead pixel of the same polarization state (or an average of equal-distant pixels). This method is easy to visualize and fast to run. However, the fidelity of the replacement is expected to be harmed by the fact that the replacing value is no nearer than $\sqrt{2}$ pixels away, as

shown in fig. 2. This greater distance can provide significant problems in areas of rapid spatial variation.

Linear DoFP polarimeters that use four measurements to estimate the three linear Stokes paramaters have the advantage of *redundancy*. The loss of a single pixel is not overly detrimental, as the intensity at that pixel can be estimated by using the other three measurements in the superpixel. We developed the expressions for this RE method, and demonstrated the superior performance when compared with the NLPN scheme for a typical LWIR polarimetric image.

The polarimetric redundancy of this polarimeter device enabled the RE scheme to be used to developed. If only three measurements had been made instead of four, then "complete" replacement could not be accomplished[1] If instead of a linear polarimeter we had used the four pixels to make four independent measurements in an attempt to reconstruct the full Stokes vector[6, 16], then we would no longer be overdetermined. Such a case is not completely hopeless. It has been shown that four independent polarization measurements within the Poincarè sphere cannot be completely orthogonal [10]. This means that the missing measurement may still be partially correlated with the other three measurements if the states are chosen properly.

The RE DPR method described here has another potential impact. One of the inherent difficulties associated with the DoFP method is the IFOV error that is inherent in the design. Many methods have been developed to mitigate these effects that are based on interpolation strategies [6, 12]. The RE DPR scheme might be adapted to allow the IFOV problems to be corrected using nearby pixels that *are not* of the same polarization, unlike previous interpolation methods that have been presented. This is the subject of future work.

[1] Complete replacement is really only possible in areas of the image that are spatially flat.

Unpolarized Calibration and Nonuniformity Correction for LWIR Microgrid Imaging Polarimeters

David L. Bowers[a], James K. Boger[a], L. David Wellems[a], Wiley T. Black[a], Steve E. Ortega[a], Bradley M. Ratliff[a], Matthew P. Fetrow[b], John E. Hubbs[c] and J. Scott Tyo[d]
[a]Applied Technology Associates, 1300 Britt St. SE, Albuquerque, NM 87123 USA
[b]Air Force Research Laboratory/VSSS, 3550 Aberdeen SE, Kirtland AFB, NM 87117
[c]Air Force Research Laboratory/VSSS, Infrared Radiation Effects Laboratory, Ball Aerospace & Technologies Corp., P.O. Box 5209, Albuquerque, New Mexico 87185
[d]College of Optical Sciences, University of Arizona, Tucson, AZ 85721, Albuquerque, NM 87131-1356 USA

ABSTRACT

Recent developments for Long Wave InfraRed (LWIR) imaging polarimeters include incorporating a micro-grid polarizer array onto the focal plane array (FPA). Inherent advantages over other classes of polarimeters include rugged packaging, inherent alignment of the opto-mechanical system, and temporal synchronization that facilitates instantaneous acquisition of both thermal and polarimetric information. Pixel-to-pixel instantaneous field-of-view (IFOV) error that is inherent in the microgrid strategy leads to false polarization signatures. Because of this IFOV error, residual pixel to pixel variations in the gain corrected responsivity, the noise equivalent input, and variations in the pixel to pixel micro-polarizer performance are extremely important. The Degree of Linear Polarization is highly sensitive to these parameters and is consequently used as a metric to explore instrument sensitivities. In this paper we explore the unpolarized calibration issues associated with this class of LWIR polarimeter and quantify the resulting false polarization signature for thermally flat test scenes.

Keywords: Infrared Polarimetry, Polarimeter, Microgrid Polarimeters

1. INTRODUCTION

Imaging polarimetry has emerged as a powerful remote sensing tool that can augment conventional intensity and spectral imagery.[1] Polarimeters have been constructed in all regions of the optical and infrared spectrum, and have been shown to aid in a number of remote sensing applications. Polarimetry provides information about surface orientation and material properties, and polarimetric data are therefore often uncorrelated with spectral and intensity data from the same scene. This fact has been exploited to defeat clutter,[2] aid in the defeat of scatterers,[3,4] and identify target composition[5] and orientation.[6]

Polarimetry in various regions of the specrum provides different information about the targets and scenes of interest.[1] In the long-wave infrared (LWIR, 8 –12 μm), polarimeters have the advantages of day/night operation. There has been interest in imaging polarimetry in the LWIR for over 20 years,[7] and many instruments have been developed to exploit this regime. In the LWIR the sources of radiation tend to be emissive, often resulting in low degrees of polarization in the imagery. In many cases, the emissive objects that make up the scene are in thermal equilibrium with the background, which has the effect of eliminating the polarization signature.[8] Furthermore, LWIR focal plane arrays (FPAs) are extremely costly, and suffer from large amounts of spatial nonuniformity (NU). This NU noise complicates polarimetric measurements much more than conventional intensity imagery, and the effects of NU noise depend on the specific architecture used for the polarimeter.[9,10]

Recent advances in LWIR detector technology have enabled the development of FPAs that are integrated with an array of micropolarizers at the pixel level. We call such devices microgrid polarimeters, and the general architecture has been used in all regions of the optical spectrum.[11] These devices have been demonstrated to provide near-real-time LWIR polarization imagery that is inherently temporally synchronized. In this paper, we discuss the effects of the unpolarized, radiometric calibration and NU correction (NUC) scheme on the thermal and polarimetric accuracy in a LWIR division of focal plane polarimeter (DoFP). DoFP devices make polarization measurements by integrating a micropolarizer array with the FPA so that neighboring pixels each see a different polarization state, as shown in fig. 1.[11]

The remainder of this paper is organized as follows. Section 2 describes the polarization measurement model we use in this study. Section 3 describes the calibration procedure. Section 4 presents experimental results with associated errors and artifacts. Section 5 concludes the paper and discusses future work.

2. POLARIZATION MEASUREMENT

Multiple intensity measurements are required to determine the polarization state of light.[12] These multiple measurements can be made sequentially in time using a single detector (or array of detectors for imaging polarimetry), or they can be made simultaneously using several detector arrays located at different physical positions. Numerous strategies have been developed to affect the simultaneous measurements, as discussed in a recent review article.[1]

One approach that has been developed for rapid acquisition of polarimetric data is to place polarization filters directly on individual detector elements of the FPA.[11] This advanced FPA technology allows simultaneous collection of data sets associated with each of the polarizer orientations in the array. The specific instrument that we are working with is a 680 x 480, engineering-grade [**BOWERS: Engineering grade means that it's not available for sale. Ernie told me to describe it this way**], HgCdTe FPA manufactured by DRS Sensors and Targeting Systems operating in the band 8–10 μm. The FPA has an integrated wire grid polarizer array that is aligned and cemented to the FPA.[13] The polarizer arrangement forms an alternating pattern of 0, 45, 90, and 135 degree orientations as shown in fig. 1, and the measured intensity data is processed to estimate the first three (s_0, s_1, s_2) Stokes parameters.[14] In principle only three measurements are necessary, but the fourth measurement provides robustness, reduces noise, and fits well with the rectangular nature of the FPA pixel pattern.[15–17] The polarization estimate is reconstructed at the intersection of the four pixels that compose a single sub-quad of pixels or a "super pixel" as depicted in Fig. 2 using one of several interpolation strategies.[18] These polarized FPA's allow for direct replacement of existing thermal FPA's, augmenting the thermal imagery by providing additional information in real time.

In this paper, we will define the Stokes vector in radiance units as*

$$\mathbf{S} = \begin{bmatrix} s_0 \\ s_1 \\ s_2 \end{bmatrix} = \begin{bmatrix} L_0 + L_{90} \\ L_0 - L_{90} \\ L_{45} - L_{135} \end{bmatrix}, \tag{1}$$

*The Stokes parameters are properly defined in terms of the statistical second moments of the electric field.[14] However, since the square of the electric field is proportional to any power or energy unit, we can easily relate our definition back to the more proper one of Stokes.

where L_0, L_{45}, L_{90}, L_{135} are the measured radiances impinging on each of the elements of a super pixel. The Stokes parameters may be used to determine the degree of linear polarization (DoLP)

$$\text{DoLP} = \sqrt{\frac{s_1^2 + s_2^2}{s_0^2}}. \tag{2}$$

The unpolarized, or radiometric, calbration of the polarimeter allows the conversion of the direct output of the pixels on the FPA to the radiance units that we have used in (1).

Ideally the component radiances in (1) would be taken at a single pixel that is aligned. However, the microgrid method forces the component radiances to be measured at offset positions as shown in fig. 2. This offset results in instantaneous field-of-view (IFOV) error, and many techniques have been explored to mitigate it.[11,18] Because of the small polarization signals and the spatial differencing inherent in (1), polarization products including DoLP are more sensitive to NUC than is thermal imagery. Consequently, we use the DoLP as a primary metric for gauging the camera polarimetric sensitivity.

3. INSTRUMENT CALIBRATION MODEL

A brief discussion of the calibration model is useful in highlighting the sensitivities of this camera. The model used for calibration is

$$R(i,j) = g(i,j)\left[\hat{\mathbf{S}}_D(i,j) \cdot \mathbf{S}(i,j)\right] + o(i,j). \tag{3}$$

$R(i,j)$ represents the response of the $(i,j)^{\text{th}}$ pixel in digital counts integrated over a finite time. The gain and offset of each pixel is $g(i,j)$ and $o(i,j)$. The radiance that finally impinges on the photodetector is given by taking the dot-product of the unknown incident Stokes vector with the dimensionless diattenuation Stokes vector of that pixel's polarizer $\hat{\mathbf{S}}_D$[†] The input has units of radiance, [W/cm^2/sr], where the spectral content of the source is integrated over the response of the pixel. Gain has units which convert radiance to counts, and the offset is in digital counts. Note that the throughput of the imaging system specified by the area of the pixel and the solid angle of acceptance of the optic are included in $G(i,j)$. This allows us to include spatially varying properties of the optical system such as vignetting in the model. The assumption of linear response of the camera detectors to photon input is known to be an approximation.

Equation (3) might be considered adequate for use in (1) by assuming ideal polarimetric properties from the microgrid array. Here, the detection model is expanded for inclusion of the wiregrid analyzer by using the appropriate Mueller matrix to represent the action of the analyzer. Using the four nearest detector elements to reconstruct a Stokes vector estimate at a given node, the matrix form for the modeled response of the super-pixel is

$$\begin{bmatrix} R_{90}(i,j) - o(i,j)_{90} \\ R_{135}(i,j) - o(i,j)_{135} \\ R_{45}(i,j) - o(i,j)_{45} \\ R_0(i,j) - o(i,j)_0 \end{bmatrix} = \begin{bmatrix} g\alpha_{90} & g\alpha_{90}\frac{\Gamma_{90}-1}{\Gamma_{90}+1}\cos 2\phi_{90} & g\alpha_{90}\frac{\Gamma_{90}-1}{\Gamma_{90}+1}\sin 2\phi_{90} \\ g\alpha_{135} & g\alpha_{135}\frac{\Gamma_{135}-1}{\Gamma_{135}+1}\cos 2\phi_{135} & g\alpha_{135}\frac{\Gamma_{135}-1}{\Gamma_{135}+1}\sin 2\phi_{135} \\ g\alpha_{45} & g\alpha_{45}\frac{\Gamma_{45}-1}{\Gamma_{45}+1}\cos 2\phi_{45} & g\alpha_{45}\frac{\Gamma_{45}-1}{\Gamma_{45}+1}\sin 2\phi_{45} \\ g\alpha_0 & g\alpha_0\frac{\Gamma_0-1}{\Gamma_0+1}\cos 2\phi_0 & g\alpha_0\frac{\Gamma_0-1}{\Gamma_0+1}\sin 2\phi_0 \end{bmatrix} \begin{bmatrix} s_0 \\ s_1 \\ s_2 \end{bmatrix}. \tag{4}$$

[†]The diattenuation Stokes vector provides the polarization state that passes the polarizer with maximum intensity. It is equal to the transpose of the first row of the polarizer Mueller matrix.[1,12]

The notation of Eq. (4) is explained with reference to Fig. 2 where i and j indicate the position in the array for the reconstructed pixel or equivalently the center of the super-pixel, while the subscript indicates the specific pixel within the super-pixel. Technically the (i,j) notation should also be attached to all of the terms within the matrix but were dropped for compactness. Three new terms have been introduced in Eq. (4): Γ_x, α_x and ϕ_x. These are specific parameters for each wiregrid analyzer and represent the extinction ratio, the net optical transmission and polarization orientation respectively. The parameter α_x is the sum of the transmission coefficients for aligned and crossed polarization typically used in the Mueller matrix for a polarizer. The net optical transmission and the gain always appear together so they can be thought of simply as the cumulative gain of the pixel that we define as

$$G(i,j) = g(i,j)\alpha(i,j). \tag{5}$$

Inverting the matrix in Eq. (4) then completes the model by which measurements can be processed to estimate the Stokes vector.

The system as presented in (4) combines the effects of the radiometric calibration with the polarimetric calibration. We can disentangle these effects by recasting (4) as

$$\begin{bmatrix} \frac{1}{G_{90}}(R_{90}-o_{90}) \\ \frac{1}{G_{135}}(R_{135}-o_{135}) \\ \frac{1}{G_{45}}(R_{45}-o_{45}) \\ \frac{1}{G_0}(R_0-o_0) \end{bmatrix} = \begin{bmatrix} 1 & \left(\frac{\Gamma_{90}-1}{\Gamma_{90}+1}\right)\cos 2\phi_{90} & \left(\frac{\Gamma_{90}-1}{\Gamma_{90}+1}\right)\sin 2\phi_{90} \\ 1 & \left(\frac{\Gamma_{135}-1}{\Gamma_{135}+1}\right)\cos 2\phi_{135} & \left(\frac{\Gamma_{135}-1}{\Gamma_{135}+1}\right)\sin 2\phi_{135} \\ 1 & \left(\frac{\Gamma_{45}-1}{\Gamma_{45}+1}\right)\cos 2\phi_{45} & \left(\frac{\Gamma_{45}-1}{\Gamma_{45}+1}\right)\sin 2\phi_{45} \\ 1 & \left(\frac{\Gamma_0-1}{\Gamma_0+1}\right)\cos 2\phi_0 & \left(\frac{\Gamma_0-1}{\Gamma_0+1}\right)\sin 2\phi_0 \end{bmatrix} \begin{bmatrix} s_0 \\ s_2 \\ s_2 \end{bmatrix}. \tag{6}$$

By casting the problem in this way, we see that the left-hand side of (6) contains all of the radiometric calibration terms and the right-hand side contains all of the polarimetric calibration terms. In this paper, we focus on the radiometric calibration of the focal plane and the resulting thermal and polarimetric errors that are introduced. Measurement sensitivities arise due to the linear model limitations and errors/variability in estimating the calibration coefficients of Eq. (4). The polarimetric calibration refers to the measurements of $\Gamma(i,j)$ and $\phi(i,j)$ for every pixel. This is a complicated measurement problem, and is discussed elsewhere.[19] Incorporating these measurement into a fully polarimetric calibration is the subject of future work.

IR focal plane arrays require non-uniformity correction (NUC) for imaging applications.[20] Standard NUC techniques include one and two point corrections. One point corrections assume that $o(i,j)$ is zero (or some other known value), and measure the response at a known temperture in order to compute $G(i,j)$. Two-point calibration schemes measure the response at two known temperatures and then estimate G and o at each pixel through linear regression. Multi-point calibrations extend this process to a piecewise-linear approximation to the true nonlinear pixel response.

Fig. 3 presents thermal (s_0) and DoLP imagery of a high-emissivity sphere is shown. These images demonstrate the increases sensitivity of the polarization products to residual NU noise. The sphere is a convenient test object, as it provides most states of linear partial polarization (up to about 10% DoLP) in a single image.[13] The constantly varying thermal and polarimetric signals across the sphere make for a challenging measurement. We use less complex target sets to quantify polarization sensitivities due to NUC methods and temperatures. Specifically we analyze spatially flat unpolarized and polarized images.

Unpolarized calibration is aimed at determining the gain and offset terms of Eq. (3). Using the linear detector model, the two point NUC is a standard method for obtaining $G(i,j)$ and $o(i,j)$, i.e.,

$$G(i,j) = \frac{R_W(i,j) - R_C(i,j)}{L_W - L_C} \tag{7}$$

and

$$o(i,j) = L_W(i,j) - G(i,j)L_W, \tag{8}$$

where $R_W(i,j)$ and $R_C(i,j)$ are the pixel responses (in counts) from warm and cool calibration sources and L_W and L_C are the associated radiances of the warm and cool calibration sources (assumed known). Digital counts are converted back to the radiance coming from the projected pixel as

$$s_0(i,j) = \frac{R(i,j) - o(i,j)}{G(i,j)}, \tag{9}$$

4. CALIBRATION ARTIFACTS IN POLARIZED DATA

Figure 4 shows representative camera digital count data from a linearity test in which the blackbody (BB) radiance is varied. For this test, an extended area BB fills the sensor's field of view (FOV) and multiple frames are collected at each radiance level. The plotted data represent the temporal average of 100 frames in order reduce temporal noise. The average value across the array for each polarizer orientation are shown with $\pm\sigma$ error bars. Non-linear saturation effects near 85° C or 23.5 $W/m^2/sr/\mu$m are evident.

This raw count data is used to demonstrate that the NUC method and calibration points affect the resultant polarization measurement. Figure 5 shows two sets of results based on different two point temperature corrections. Figures 5.a and 5.b show that the s_0 error increases away from the NUC temperature points as evident by the expanding error bars. As illustrated in Fig. 5.c and 5.d this residual non-uniformity results in errors in the scene polarization estimates. At the NUC temperatures, there is no error in either s_0 or DoLP, as expected.

The effect of the unpolarized calibration method on the polarization products is more complex. For these flat scenes, both s_1 and s_2 should be exactly zero. However, polarization artifacts begin to appear, such as the unbalanced error in s_1 and s_2 away from the NUC temperatures. This effect can be explained by the average response differences due to variations in microgrid polarizer performance and pixel response that are shown in in Fig. 4. The difference in the means between the 45° and 135° orientations is greater than the difference of the means of the 0° and 90° orientations. The 135° orientation also shows the greatest spatial nonuniformity, resulting in the larger error bars for s_2.

In conventional, non-polarized imagery the operator usually attempts to choose NUC temperatures that bound the scene temperatures as closely as possible. Bounding a polarized scene using an optimal two point NUC is more complicated. Pixels with polarizers that are perpendicular to the incoming state of polarized light will have low radiance levels reaching the pixel, especially for scenes with significant DoLP. The radiance transmitted through the polarizer given by $\left[\hat{\mathbf{S}}_D \cdot \mathbf{S}\right]$ in (3) for a pixel with a perpendicular state may result in the pixel operating in a non-linear response regime of the pixel. The residual spatial nonuniformity and resulting DoLP estimates depend on the NUC temperatures and scene temperatures. Low extinction ratios are actually beneficial in two point gain and offset calibration because the throughput radiance remains in a narrower range, helping the camera to stay closer to its

NUC temperatures. So long as Γ is well calibrated, it has no effect on the accuracy of the polarimeter, and only limited effect on the SNR.[21]

Figure 6 shows how the DoLP magnitude estimates vary with NUC temperature to polarized 'flat' fields. These scenes were generated using an extended BB behind a wire grid polarizer (WGP) placed to fill the sensor's FOV. The state of polarization was controlled by rotating the WGP. The DoLP was controlled by changing the BB temperature which varies the balance of radiation transmitted through the WGP from the BB and radiation reflected off the WGB from the background. If the BB is at the same temperature as the ambient, then the transmitted and reflected radiances are equal, and the resulting total field is unpolarized. Two different sets of two point NUC temperatures were used to correct the data.

The DoLP variations with these NUC temperatures are displayed graphically on the Poincaré disk[‡]. At first glance, it is reasonable to assume that the larger s_0 estimate in Fig. 6.a for the 50, 100° C case is causing the normalized s_1 and s_2 values in Fig. 6.b to be smaller. However, the same trend is evident when plotting the non-normalized s_1 and s_2 values, that is, the lower two point NUC temperatures are yielding larger estimates of s_1 and s_2.

A look at the gain and offset histograms of Fig. 7 explains the systematic affect. The smaller gain estimate generated in the 15, 50° C case leads to a larger offset estimate. When this larger offset is subtracted from the input the resultant s_1 and s_2 estimates are larger. Conversely, when smaller offset is subtracted from the input, the s_1 and s_2 estimates are smaller. In each case, unless a perfect calibration is obtained, the offset is not being accounted for properly and is acting to increase or decrease the thermal and polarization estimates. Shot to shot variance and drifts in the calibration sources and sensor lead to difficulties in the radiometric calibration and consequently the polarimetric estimates. Bounding the scene is problematic and depends on the temperature variation and polarization in scene.

5. CONCLUSIONS

In this paper, we have discussed the effects of unpolarized calibration on the performance of a LWIR imaging polarimeter built with the DoFP architecture. We see that the performance of the FPA is sensitive for both the unpolarized (s_0) and polarized (s_1 and s_2) channels. However, residual calibration error has a much larger effect on the resulting polarization products. Calibration of the camera system involves measuring not only the pixel photoresponse, but also the properties of the micropolarizer array.

This paper only considers the unpolarized aspects of the calibration process. Use of a fully calibrated data reduction matrix (DRM)[12] will enhance the performance, but characterization of the DRM is complicated for this class of sensor. Discussion of the DRM for this instrument is the subject of a future paper.

6. ACKNOWLEDMENTS

The authors would like to acknowledge Robert Mack of AFRL/SNJT for collaboration on and continued use of a LWIR microgrid sensor. J. S. Tyo and J. K. Boger were supported in part by the Air Force Office of Scientific Research under award #FA9550-05-1-0090 and the National Science Foundation under award # 0238309.

[‡]We define the Poincarè disk as the equatorial plane of the Poincarè sphere.

REFERENCES

1. J. S. Tyo, D. H. Goldstein, D. B. Chenault, and J. A. Shaw, "Review of passive imaging polarimetry for remote sensing applications," *Appl. Opt.* **45**, pp. 5453 – 5469, August 2006.
2. L. J. Cheng, M. Hamilton, C. Mahoney, and G. Reyes, "Analysis of aotf hyperspectral imaging," in *Proceedings of SPIE Vol. 2231, Algorithms for Multispectral and Hyperspectral Imagery*, A. Iverson, ed., pp. 158–166, SPIE, (Bellingham, WA), 1994.
3. J. S. Tyo, M. P. Rowe, E. N. Pugh, and N. Engheta, "Target detection in optically scattering media by polarization-difference imaging," *Appl. Opt.* **35**, pp. 1855–1870, 1996.
4. D. B. Chenault and J. L. Pezzaniti, "Polarization imaging through scattering media," pp. 124 – 133, SPIE, (Bellingham, WA), 2000.
5. L. B. Wolff and T. E. Boult, "Constraining object features using a polarization reflectance model," *IEEE Trans. Patt. Analysis Machine Intell.* **13**, pp. 635–657, 1991.
6. L. B. Wolff, "Surface orientation from polarization images," in *Proceedings of SPIE vol. 850 Optics, illumination, and image sensing for machine vision II*, D. J. Svetkoff, ed., pp. 110–121, SPIE, (Bellingham, WA), 1987.
7. T. J. Rogne, "Passive detection using polarized components of infrared signatures," in *Proceedings of SPIE vol. 1317: Polarimetry: Radar, infrared visible, ultraviolet and X-ray*, R. A. Chipman and J. W. Morris, eds., pp. 242 – 251, SPIE, (Bellingham, WA), 1990.
8. J. S. Tyo, J. K. Boger, B. M. Ratliff, W. T. Black, D. L. Bowers, and M. P. Fetrow, "The effects of thermal equilibrium and thermal contrast in polarimetric images in the lwir," *Opt. Express* . Submitted, November 2006.
9. B. M. Ratliff, *A Generalized Algebraic Scene-based Nonuniformity Correction Algorithm for Infrared Focal Plane Arrays.* PhD thesis, University of New Mexico, 2004. Electrical and Computer Engineering Department.
10. B. M. Ratliff, R. Kumar, J. S. Tyo, and M. M. Hayat, "Combatting infrared focal plane array nonuniformity noise in imaging polarimeters," in *Proc. SPIE vol. 5888: Polarization Science and Remote Sensing II*, J. A. Shaw and J. S. Tyo, eds., p. 58880J, SPIE, (Bellingham, WA), 2005.
11. A. G. Andreou and Z. K. Kalayjian, "Polarization imaging: principles and integrated polarimeters," *IEEE Sensors Journal* **2**, pp. 566 – 576, 2002.
12. R. A. Chipman, "Polarimetry," in *Handbook of Optics*, M. Bass, ed., **2**, ch. 22, McGraw-Hill, 1995.
13. D. Bowers, J. K. Boger, L. D. Wellens, W. T. Black, S. E. Ortega, B. M. Ratliff, M. P. Fetrow, J. E. Hubbs, and J. S. Tyo, "Evaluation and display of polarimetric image data using long-wave cooled microgrid focal plane arrays," in *Proc. SPIE vol. 6240: Polarization: Measurement, Analysis, and Remote Sensing VII*, D. H. Goldstein and D. B. Chenault, eds., p. 6240OF, SPIE, (Bellingham, WA), 2006.
14. R. M. A. Azzam and N. M. Bashara, *Ellipsometry and Polarized Light*, North-Holland, New York, 1977.
15. R. Walraven, "Polarization imagery," *Opt. Eng.* **20**, pp. 14 – 18, 1981.
16. J. S. Tyo, "Optimum linear combination strategy for a N-channel polarization sensitive vision or imaging system," *J. Opt. Soc. Am. A* **15**, pp. 359–366, 1998.
17. J. S. Tyo, "Design of optimal polarimers: maximization of SNR and minimization of systematic errors," *Appl. Opt.* **41**, pp. 619–630, 2002.
18. B. M. Ratliff, J. K. Boger, M. P. Fetrow, J. S. Tyo, and W. T. Black, "Image processing methods to compensate for ifov errors in microgrid imaging polarimeters," in *Proc. SPIE vol. 6240: Polarization: Measurement, Analysis, and Remote Sensing VII*, D. H. Goldstein and D. B. Chenault, eds., p. 6240OE, SPIE, Bellingham, WA, 2006.
19. J. E. Hubbs, M. E. Gramer, D. Maestas-Jepson, G. A. Dole, M. P. Fetrow, D. L. Bowers, J. K. Boger, and E. Atkins, "Measurement of the radiometric and polarization characteristics of a microgrid polarizer infrared focal plane array," in *Proceedings of SPIE vol. and 6295: Infrared Detectors and Focal Plane Arrays VIII*, E. L. Dereniak and R. E. Sampson, eds., p. 62950C, SPIE, (Bellingham, WA), 2006.
20. D. L. Perry and E. L. Dereniak, "Linear theory of nonuniformity correction in infrared staring sensors," *Opt. Eng.* **32**, pp. 1854–1859, 1993.

21. J. S. Tyo and H. Wei, "Imaging polarimetry with imperfect optics," *Appl. Opt.* **45**, pp. 5497 – 5503, August 2006.

Figure Captions

Fig. 1: Division of Focal Plane (DoFP) polarimeters operate by placing a micropolarizer in front of each pixel that analyzes a different polarization state. Stokes vectors are estimated at interpolation points as shown in the figure.[13]

Fig. 2: Super-pixel of the microgrid polarimeter.

Fig. 3: DoLP imagery is more sensitive to NUC than thermal imagery.

Fig. 4: Average counts versus radiance.

Fig. 5: Linear approximation errors in $s_0, s_1/s_0$, and s_2/s_0 for unpolarized light. Calibration temperatures are indicated on the figures.

Fig. 6: Linear approximation errors in $s_0, s_1/s_0$, and s_2/s_0 to polarized light.

Fig. 7: Gain and offset variations due to NUC temperatures affect DoLP estimates.

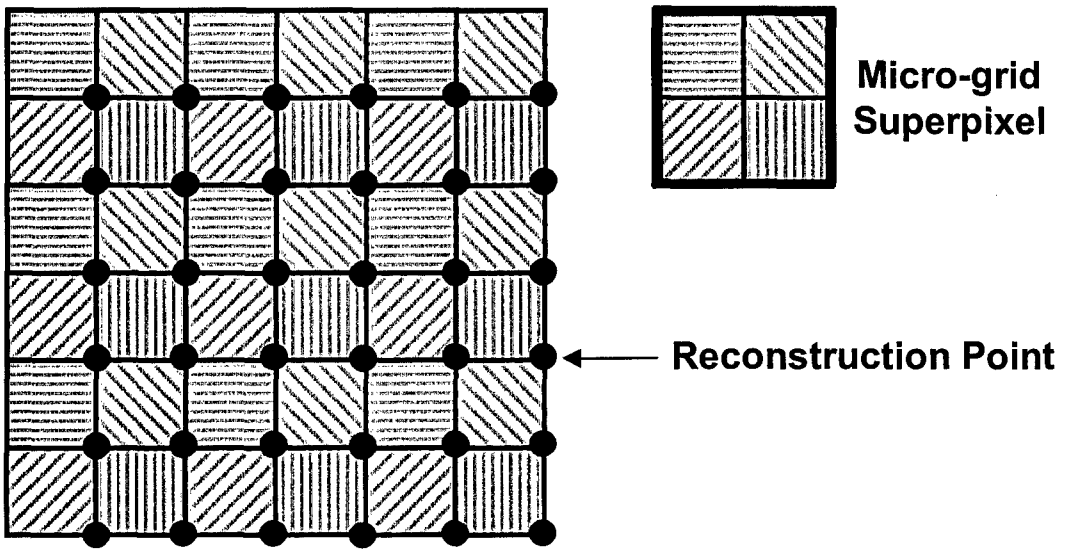

Figure 1. Division of Focal Plane (DoFP) polarimeters operate by placing a micropolarizer in front of each pixel that analyzes a different polarization state. Stokes vectors are estimated at interpolation points as shown in the figure.[13]

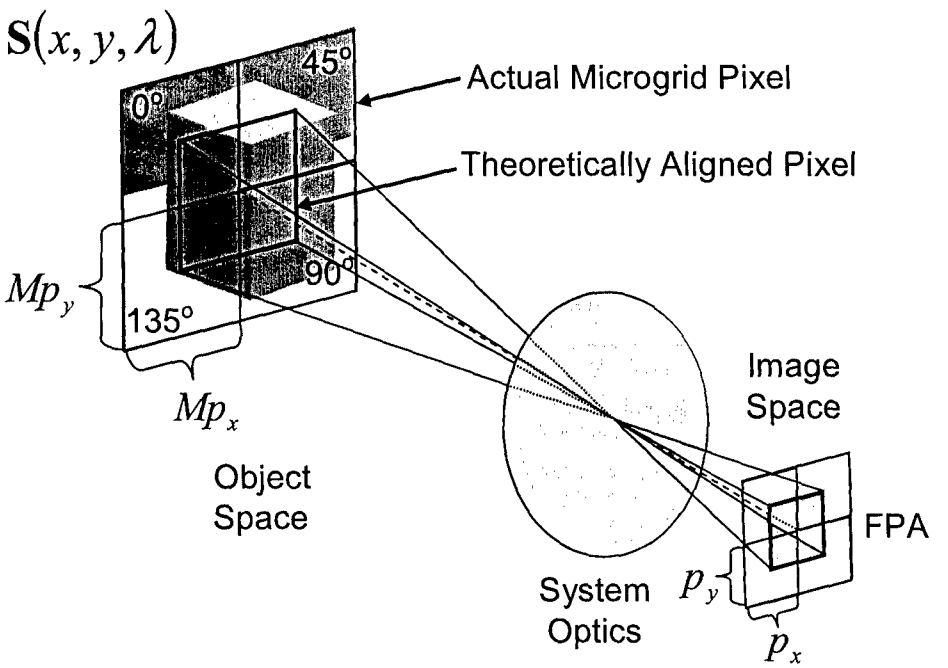

Figure 2. Super-pixel of the microgrid polarimeter.

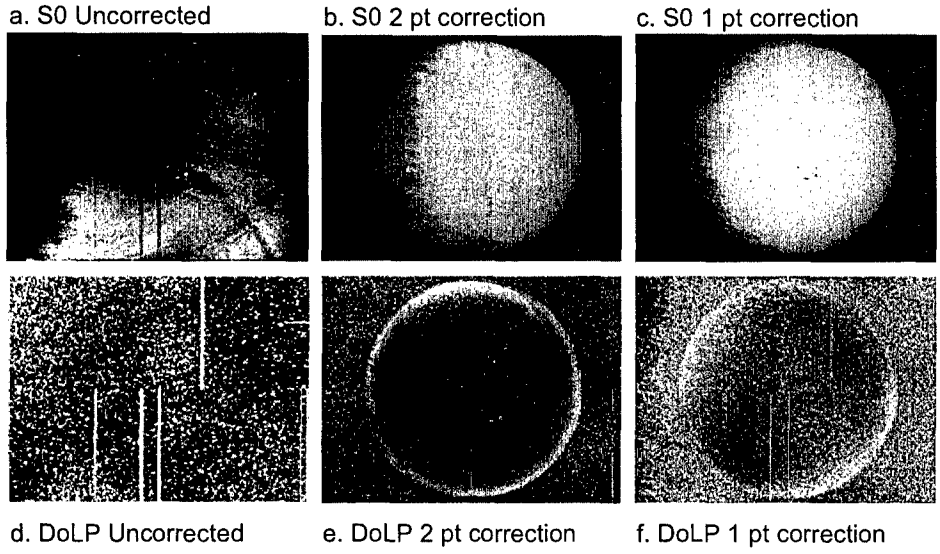

Figure 3. DoLP imagery is more sensitive to NUC than thermal imagery.

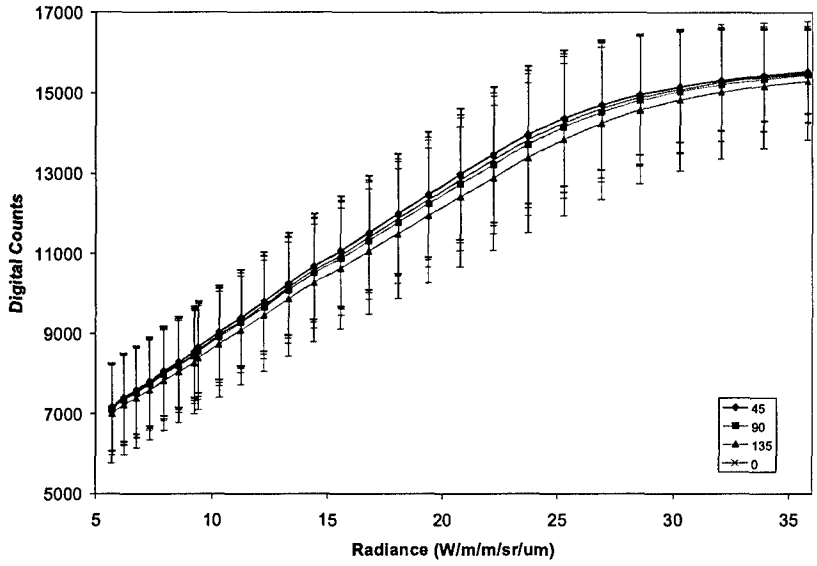

Figure 4. Average counts versus radiance.

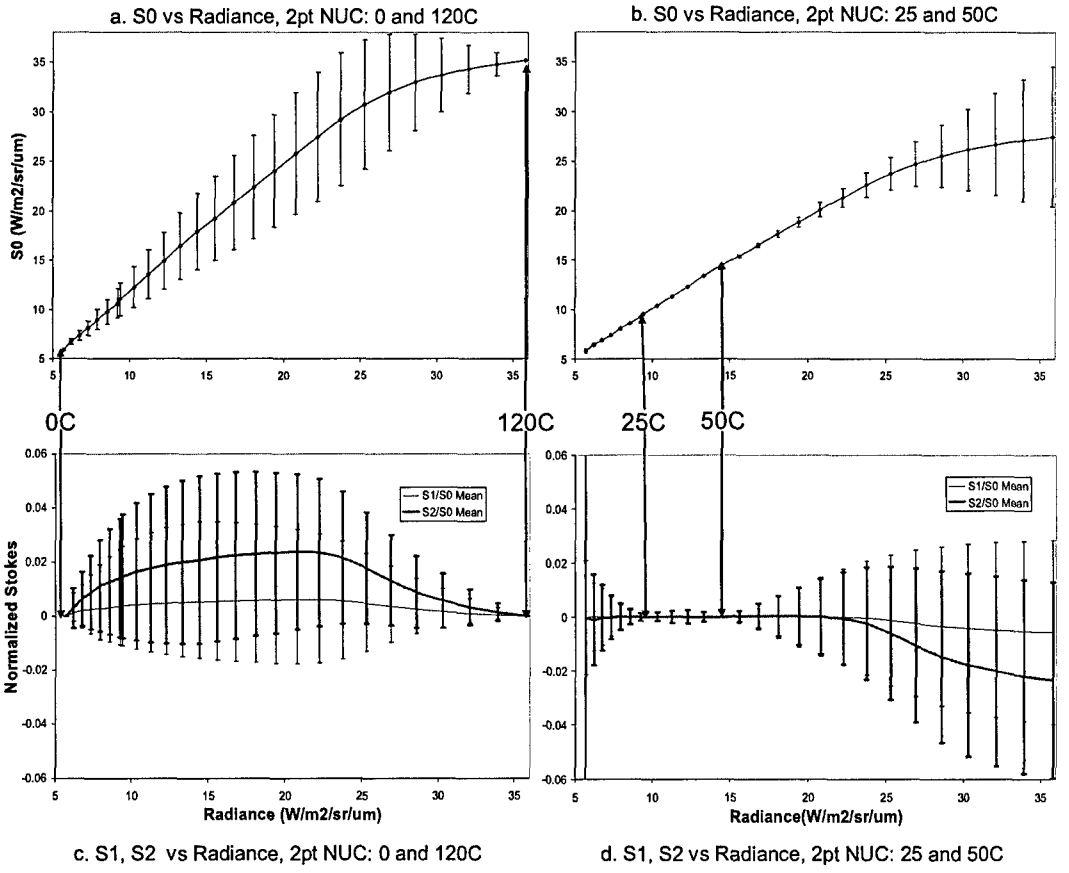

Figure 5. Linear approximation errors in $s_0, s_1/s_0$, and s_2/s_0 for unpolarized light. Calibration temperatures are indicated on the figures.

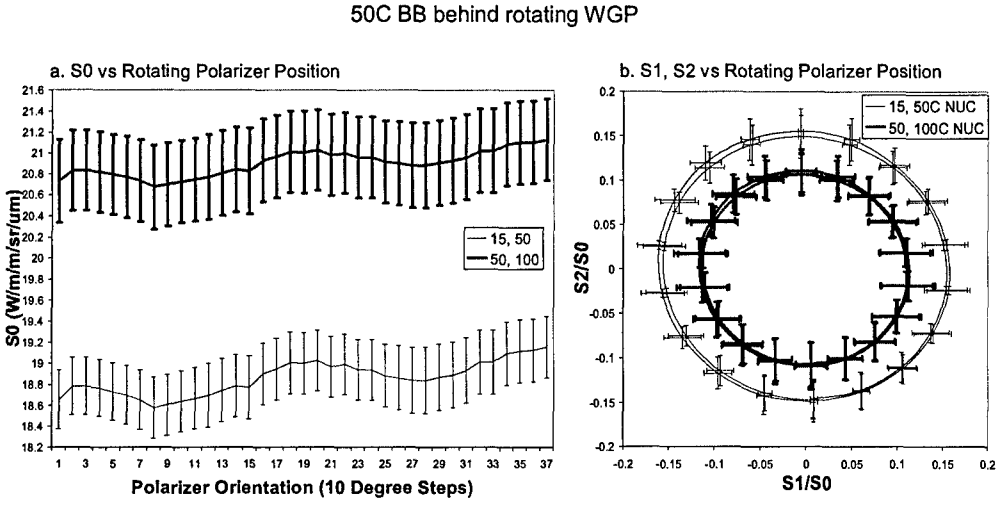

Figure 6. Linear approximation errors in $s_0, s_1/s_0$, and s_2/s_0 to polarized light.

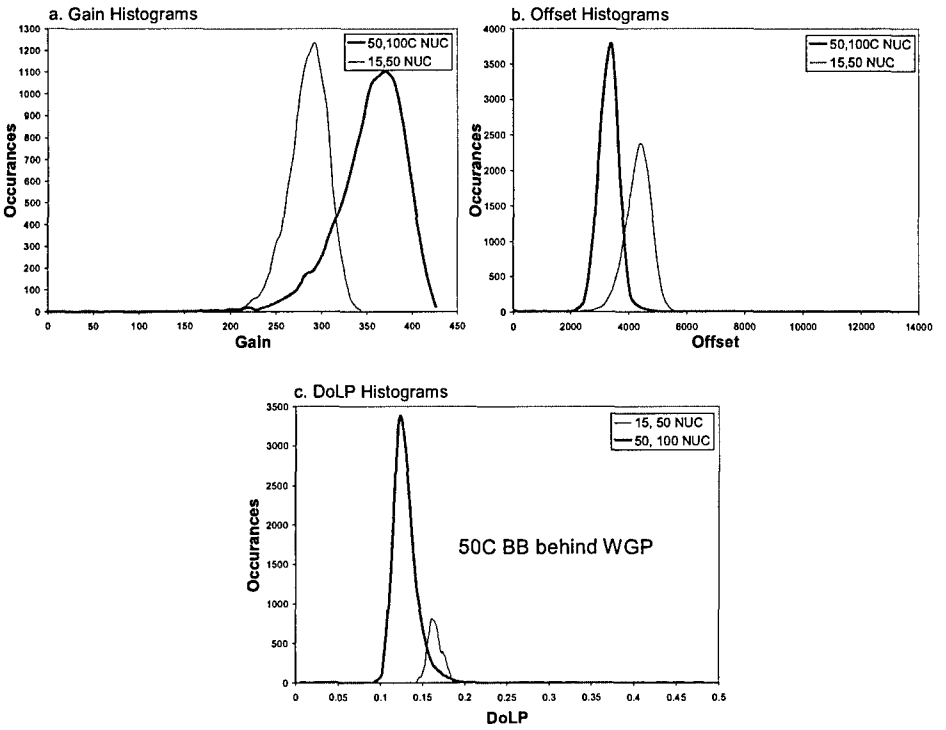

Figure 7. Gain and offset variations due to NUC temperatures affect DoLP estimates.

The Role of Polarized Calibration in the Performance of LWIR Microgrid Polarimeters

James K. Boger[a], David L. Bowers[a], Wiley T. Black[a], Steve E. Ortega[a], Bradley M. Ratliff[a], Matthew P. Fetrow[b], John E. Hubbs[c] and J. Scott Tyo[d]
[a]Applied Technology Associates, 1300 Britt St. SE, Albuquerque, NM 87123 USA
[b]Air Force Research Laboratory/VSSS, 3550 Aberdeen SE, Kirtland AFB, NM 87117
[c]Air Force Research Laboratory/VSSS, Infrared Radiation Effects Laboratory, Ball Aerospace & Technologies Corp., P.O. Box 5209, Albuquerque, New Mexico 87185
[d]College of Optical Sciences, University of Arizona, Tucson, AZ 85721, Albuquerque, NM 87131-1356 USA

ABSTRACT

Enhancing LWIR images is always desirable and adding polarimetric information is one way to do this. To realize the benefits of adding polarization to LWIR imaging, extensive calibrations are required. LWIR imaging arrays are notoriously uneven in their spatial response and require frequent sensor flat-field calibrations to maintain good imaging performance. Radiometric calibration is often done as part of the flat-fielding process. This calibration can drastically improve image quality. In addition to the sensors response to photons, LWIR microgrid instruments are sensitive to polarization. These instruments can exacerbate the non-uniform intensity response. Thus the flat-field may change due to a change in polarization of the scene. To address this a polarimetric calibration is done to spatially correct the array for polarized input. This paper first reviews the mathematics associated with the polarimetric calibration and processing, then describes two methods used to measure calibration coefficients. Calibrations are then applied to data to demonstrate the utility of the calibration and compare the methods used to collect data.

Keywords: Polarimetry, Long-wave Infrared, Microgrid, Polarimetric calibration, Image processing, Focal plane array, Remote sensing.

1. INTRODUCTION

LWIR Polarimetric imaging has been used for remote sensing applications for the purpose of image enhancement.[?,?,1–3] The enhancement often comes after extensive image processing where ultimately the polarimetric information is fused to the intensity image as illustrated in fig. 1. Getting to this image requires considerable efforts in camera construction, calibration, careful operation and imaging processing.[4] The first challenge was building a polarimetrically sensitive camera.[6] Because polarization requires multiple samples of an intensity scene under optically diverse conditions, it has been difficult to build

Figure 1. LWIR with polarization fused to intensity through a false color scheme.[5]

a stable polarimeter capable of running at video rates in the LWIR. This is because most measurement schemes rely on sequential measurements in time to build up the cache of raw data needed.[7] DRS and other companies have overcome this problem by masking each pixel in the FPA with a wire-grid polarizer,WGP, appropriately dimensioned such as to be polarizing in the choosen waveband. Sensors built in this fashion are typically referred to as microgrid arrays.

Discussion begins with a mathematical outline of the model used to process raw data into polarimetric estimates. The model is covered in some detail as it is important in understanding what is needed for polarimetric calibration coefficients. Because polarimetric and radiometric aspects of the sensor are naturally mixed, we outline how the two calibrations separate within the mathematical model. This will isolate the polarimetric portion of the model which we refer to here as the Data Reduction Matrix, **DRM**. Obtaining a calibrated **DRM** is the goal of this work. The paper then goes on to describe two methods by which the needed calibration coefficients are estimated. This is done because we have found that the measured calibration coefficients are not exact and that the polarimetric calibration will be limited by the accuracy of these data. In the simplest description, one method requires a greater level of effort and was assumed to be a better estimate. Polarimetric calibration is hoped to improve the polarimetric accuracy and improve the final image product such as that shown in Fig. 1. We conclude the paper by carefully examining the impacts of calibration on data. This is done in several different ways since no one

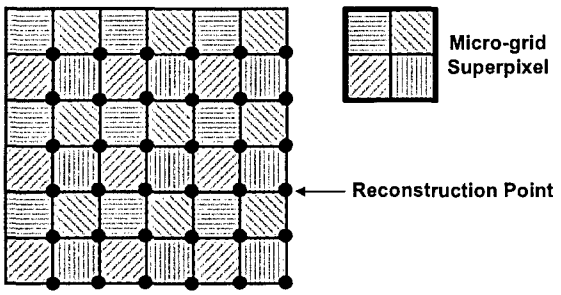

Figure 2. Microgrid pattern on FPA

metric is sufficient in gauging the multiple benefits of polarimetric calibration. The final metric is to gauge the impact of applying the calibrated **DRM** to an actual polarimetric image.

2. DERIVING THE DRM

2.1. The Stoke parameterization

All polarimeters depend on making multiple measurements of a single streaming light signal to fill out the Stokes parameterization of polarization.[7,8] In the case of the microgrid array, the diversity in measurement is achieved by making four spatially separated measurements with four individual pixels, each having a wire-grid analyzer on the pixel at a unique angle. Figure 2 illustrates a pattern of wire grids on a 4x4 section of an array.

In a linear only measurement, only 3 of the four Stokes parameters are sought. Typically, 4 linear polarization measurements nicely estimate the linear only Stokes. Thus we often speak of the sub-quad as a single polarization measurement which refers to 4 unique pixels necessary to reconstruct Stokes. As diagramed in Fig. 2, polarization is reconstructed at the intersection of the 4 pixels which compose a single sub-quad. From the figure, it is clear that every intersection contains 4 unique analyzers and as a consequence a polarization image is constructed with nearly the same resolution that the intensity image. The mathematics used to reconstruct the Stokes at a single point can be borrowed directly from the definition of the Stoke parameters:

$$\begin{bmatrix} S_0 \\ S_1 \\ S_2 \end{bmatrix} = \begin{bmatrix} I_H + I_V \\ I_H - I_V \\ I_{45} - I_{135} \end{bmatrix} \tag{1}$$

Here I_H and I_V are the horizontally and vertically polarized signals from the appropriate pixels respectively. Note that the Stokes term which parameterizes circular polarization

S_3, has been ignored. The processing is straight forward and yields a reasonable estimate of polarization. To get the degree of linear polarization, DoLP, we RSS the S_1 and S_2 terms and normalize by S_0. Using Eq. 1 as the mathematical model often produces good images. But improving accuracy and precision as well as improving the products visually, is an ongoing battle, particularly in the LWIR. Calibration is an obvious improvement but understanding it requires that we outline a more rigorous approach for the mathematical model.

2.2. Response matrix and the DRM

Our goal is to find the polarization state (less S_3) entering the sensor. We do this by combining 4 unique measurements from four pixels in a given sub-quad. Since microgrid has imperfections polarimetrically on a pixel-by-pixel basis problems can creep into the data. To expose them, it is useful to track the Stokes vector through the optical system up to the intensity detector. This is done by finding the Mueller matrix for each sensor in the array and then applying the matrix to an input Stokes vector. The true Mueller matrix would include contributions from every optical element in the path to the actual sensor. We have simplified our model to include effects of the WGP only. Since the HgCdTe array is an intensity detector, only S_0 of the input Stokes vector remains. This means that when applying the Mueller matrix, only the top row is used for each individual detection. The top row is often called the analyzer vector.[9] The combination of 4 measurements can be written in matrix formalism, where the matrix is a stack of 4 analyzer vectors, one for each pixel in the sub-quad. If we collect these analyzer vectors in this fashion, one for each pixel in a 2x2 quad, then we have in theory collected enough information to solve for the input state.[10,11] Note that the formalism can be extended beyond the 2x2 quad easily by continuing the process of stacking anaylzer vectors to include all the measurements used in a single polarization estimate.

$$\mathbf{PR} = \frac{1}{2}\begin{bmatrix} q_H + r_H & (q_H - r_H)\cos 2\phi_H & (q_H - r_H)\sin 2\phi_H & 0 \\ q_{45} + r_{45} & (q_{45} - r_{45})\cos 2\phi_{45} & (q_{45} - r_{45})\sin 2\phi_{45} & 0 \\ q_V + r_V & (q_V - r_V)\cos 2\phi_V & (q_V - r_V)\sin 2\phi_V & 0 \\ q_{135} + r_{135} & (q_{135} - r_{135})\cos 2\phi_{135} & (q_{135} - r_{135})\sin 2\phi_{135} & 0 \end{bmatrix} \tag{2}$$

The subscripts are used to identify the individual pixel, q and r represent the intensity transmission coefficients for horizontal and vertical polarization signals respectively and ϕ is the orientation of the WGP as measured from the local (sensor) horizontal. Note that we assume the Stokes vector presented to each pixel is identical, a source for error, but not one we consider here.[12] Also, the circular term S_3 is seen to be lost in this measurement prescription by the last column in the response matrix of eq. 2 and consequently S_3 is dropped.

Equation 2 less the right most column is the 3x4 matrix form for converting Stokes incident on a sub-quad to 4 individual radiant signals at the detector. The matrix itself is termed the sub-quad polarimetric response matrix, **PR**. The goal is to recover an estimate of Stokes, $\vec{S}$, given the response vector, $\vec{R}$, which contains the 4 pixel responses from a sub-quad. Mathematically this simply means inverting **PR**. Thus **DRM** is the inverse of **PR**. With the mathematical recipe in hand, it is a conceptually simple matter to account for the imperfections of each wire grid analyzer on a pixel-by-pixel basis. One need only measure the parameters q, r and ϕ for each pixel and construct the actual response matrices for the many sub-quads in the FPA. In the LWIR this is often difficult.

Before describing the measurement of q, r and ϕ, it is helpful to recast the problem in terms of extinction ratio, Γ. The reason for this is simply that the measurement scheme presented does not recover 3 independent quantities. Further, there is a practical matter concerning the gain of an individual pixel that needs to be exposed an accounted for.

Γ is the ratio of light intensities transmitted by the polarizer when its polarization axis is first aligned to the linear input state and then crossed by exactly 90 degrees. The definition of extinction ratio is $\Gamma = \frac{q}{r}$. By conservation of energy, a second relationship between q and r is that they must sum to some number α, less than 1. This is the net transmission of the optic and might be 96% for a coated optic. The measurement described here does not attempt to quantify α as it has no impact on the estimate of polarization; rather it is a radiometric concern. The α term is further addressed in section 3. With Γ and ϕ identified as our principal unknown coefficients, we recast the generic **PR** matrix in those terms.

$$\mathbf{PR} = \frac{1}{2}\begin{bmatrix} \alpha_H & \alpha_H\left(\frac{\Gamma_H-1}{\Gamma_H+1}\right)\cos 2\phi_H & \alpha_H\left(\frac{\Gamma_H-1}{\Gamma_H+1}\right)\sin 2\phi_H \\ \alpha_{45} & \alpha_{45}\left(\frac{\Gamma_{45}-1}{\Gamma_{45}+1}\right)\cos 2\phi_{45} & \alpha_{45}\left(\frac{\Gamma_{45}-1}{\Gamma_{45}+1}\right)\sin 2\phi_{45} \\ \alpha_V & \alpha_V\left(\frac{\Gamma_V-1}{\Gamma_V+1}\right)\cos 2\phi_V & \alpha_V\left(\frac{\Gamma_V-1}{\Gamma_V+1}\right)\sin 2\phi_V \\ \alpha_{135} & \alpha_{135}\left(\frac{\Gamma_{135}-1}{\Gamma_{135}+1}\right)\cos 2\phi_{135} & \alpha_{135}\left(\frac{\Gamma_{135}-1}{\Gamma_{135}+1}\right)\sin 2\phi_{135} \end{bmatrix} \tag{3}$$

3. USING THE DRM

Applying the polarimetric correction allows us to distinguish between polarimetric and radiometric corrections. Radiometric corrections in this context means calibrating for a uniform and accurate intensity response across all pixels. Note that radiometric and polarimetric parameters are mixed in eq. 3 since α affects only the radiometric signal but is contained in the **PR** matrix. Because of this we separate α from the polarimetric calibration. The Non-Uniformity Correction or NUC, is commonly used as the radiometric calibration. Radiometric response of an individual pixel can change, forcing the need for frequent NUC operations. NUCs are a regular operation for all LWIR FPA sensors and effort is made to make this correction happen quickly. The polarimetric characteristics on

the other hand, are assumed to be constant. Consequently, we believe there is no need for updating calibration coefficients in the polarimetric case. As a result, we introduce a formalizism for applying radiometric and polarimetric calibrations separately.

Sensor pixels output digital counts to the user. The translation from radiometric units to counts is captured by the gain of each pixel. The typical model used to capture this is a linear model. The real response of the sensor pixels may not be linear, but a piecewise linear model is implemented in that case and the linear model is still appropriate. Eq. 4 expresses the linear model with units given for clarity. Each pixel has a unique gain and offset which necessitates the NUC.

$$R(counts) = g\left(\frac{counts \cdot sec}{photons}\right) S_{0d}\left(\frac{photons}{sec}\right) + o(counts) \tag{4}$$

In Eq. 4, S_{0d} is the resultant signal at the detector after having passed through the optical path and WGP. The parameter g is the individual pixel gain and o is that pixel's offset. S_{0d} resulted from the input Stokes vector $\vec{S}$, being analyzed by one of the row vectors expressed in eq. 3. Combining eqs. 3 and 4 gives the complete mathematical model for our sensor.

$$\begin{bmatrix} R_H - o_H \\ R_{45} - o_{45} \\ R_V - o_V \\ R_{135} - o_{135} \end{bmatrix} = \frac{1}{2} \begin{bmatrix} g\alpha_H & g\alpha_H\left(\frac{\Gamma_H - 1}{\Gamma_H + 1}\right)\cos 2\phi_H & g\alpha_H\left(\frac{\Gamma_H - 1}{\Gamma_H + 1}\right)\sin 2\phi_H \\ g\alpha_{45} & g\alpha_{45}\left(\frac{\Gamma_{45} - 1}{\Gamma_{45} + 1}\right)\cos 2\phi_{45} & g\alpha_{45}\left(\frac{\Gamma_{45} - 1}{\Gamma_{45} + 1}\right)\sin 2\phi_{45} \\ g\alpha_V & g\alpha_V\left(\frac{\Gamma_V - 1}{\Gamma_V + 1}\right)\cos 2\phi_V & g\alpha_V\left(\frac{\Gamma_V - 1}{\Gamma_V + 1}\right)\sin 2\phi_V \\ g\alpha_{135} & g\alpha_{135}\left(\frac{\Gamma_{135} - 1}{\Gamma_{135} + 1}\right)\cos 2\phi_{135} & g\alpha_{135}\left(\frac{\Gamma_{135} - 1}{\Gamma_{135} + 1}\right)\sin 2\phi_{135} \end{bmatrix} \begin{bmatrix} S_0 \\ S_1 \\ S_2 \end{bmatrix} \tag{5}$$

The important point here is that each detector pixel has a unique α and g which always appear together. Consequently the two coefficients can be thought of as one. This is important as it reduces the number of coefficients in the model which must be measured in the calibration phase of the sensor. Since α and g are combined, a method emerges for calibration. This method is apparent when we isoloate the polarimetric response matrix from the gain of each pixel in eq. 5 such that the model equation becomes eq. 6.

$$\begin{bmatrix} \frac{1}{g\alpha_H}(R_H - o_H) \\ \frac{1}{g\alpha_{45}}(R_{45} - o_{45}) \\ \frac{1}{g\alpha_V}(R_V - o_V) \\ \frac{1}{g\alpha_{135}}(R_{135} - o_{135}) \end{bmatrix} = \frac{1}{2} \begin{bmatrix} 1 & \left(\frac{\Gamma_H - 1}{\Gamma_H + 1}\right)\cos 2\phi_H & \left(\frac{\Gamma_H - 1}{\Gamma_H + 1}\right)\sin 2\phi_H \\ 1 & \left(\frac{\Gamma_{45} - 1}{\Gamma_{45} + 1}\right)\cos 2\phi_{45} & \left(\frac{\Gamma_{45} - 1}{\Gamma_{45} + 1}\right)\sin 2\phi_{45} \\ 1 & \left(\frac{\Gamma_V - 1}{\Gamma_V + 1}\right)\cos 2\phi_V & \left(\frac{\Gamma_V - 1}{\Gamma_V + 1}\right)\sin 2\phi_V \\ 1 & \left(\frac{\Gamma_{135} - 1}{\Gamma_{135} + 1}\right)\cos 2\phi_{135} & \left(\frac{\Gamma_{135} - 1}{\Gamma_{135} + 1}\right)\sin 2\phi_{135} \end{bmatrix} \begin{bmatrix} S_0 \\ S_1 \\ S_2 \end{bmatrix} \tag{6}$$

We have intentionally omitted the standard indexing notation, (i,j), because of the confusion between reconstructed pixels and real pixels. Instead we keep with one sub-quad for illustrative purposes. With measured Γ and ϕ for each pixel, this becomes the calibrated **PR** matrix. To use eq. 6 we would NUC the array or radiometrically calibrate all of the responses, then multiple by the inverse of the polarimetric response matrix given. In other words, the lhs of eq. 6 is the radiometric correction of the responses and the rhs is the polarimetric processing.

4. MEASURING WIRE GRID POLARIZER PARAMETERS

Because the value of the calibration is critically dependent on good measurements of the parameters of the microgrid, we present two different measurements as well as the results of applying these calibrations to data. The techniques are similar, differing primarily in level of effort to accurately measure the calibration parameters. Both measurement schemes use a sequence of input polarization states which are then modulated according to Malus's law by the sensor. The first technique is a responsivity measurement and the second is a differencing and modulation measurement. Because the first technique is a direct measurement, the polarization state generator is cooled to control background radiance levels. By contrast, the second technique is a relative measurement where differencing and Fourier demodualtion are used to deal with experimental problems such as a warm polarization state generator. Sections 4.1 and 4.2 discuss the two techniques and the resulting data. We conclude that the measurements are the limiting factor in the quality of the calibration but it is not a simple matter to dramatically improve them.

4.1. Method 1: Responsivity Measurements

Method 1 was used at the Air Force Research Laboratory in the IR Radiation Effects Lab (IRREL) and has been published.[13] The technique of analyzing the responsivity was natural because the chip was being radiometrically characterized at the time these polarimeteric measurements were made. Much of the discussion here is covered in the reference with more detail.

4.1.1. Experimental Setup for Responsivity Measurements

The first polarization characterization measurement was made with the FPA mounted in liquid helium pour-filled cryogenic dewars as shown in Figure 3. A field-of-view limiting aperture and a Thor Laboratory polarizer, both mounted on a liquid helium cold shield, set the background photon irradiance on the FPA. The polarizer was designed to rotate its position about the optical axis in 22.5 increments. In addition, a cold spectral filter that was mounted on the liquid nitrogen cold shield limits the spectral content of the photon irradiance. An external blackbody was used as the source of signal irradiance. For the geometry used, the field-of-view of all pixels was filled by the blackbody.

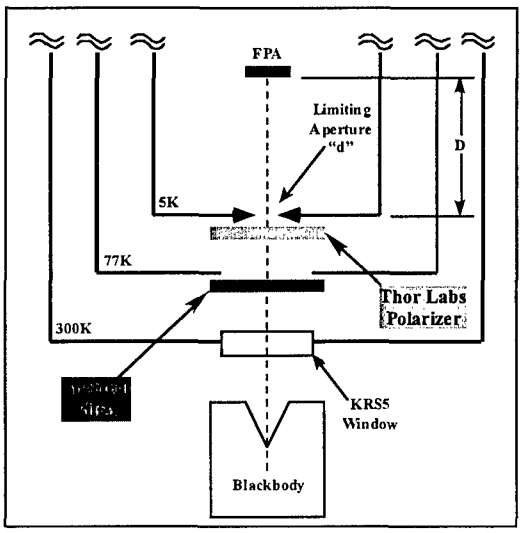

Figure 3. Law of Malus arrangement used to collect ER and orientation calibration data

4.1.2. Signal Photon Irradiance

Signal photon irradiances were calculated using a numerical integral of the product of the detector spectral response, the pixel field-of-view, the spectral distribution of the photon exitance from the blackbody, and the spectral transmittance of the spectral filter and the vacuum window, as given by Eq. 7. Note that the transmission characteristics of the Thor Laboratory polarizer are not taken into account by this calculation because the microgrid filters consists of four different orientations: horizontal, vertical, 45^o, and 135^o. By excluding the polarizer from the calculation, the measured responsivity will include the convolution of the microgrid filters with the Thor Laboratory polarizer. All blackbody photon irradiances are referred to the center of spectral filter pass-band. By using various blackbody temperatures, a wide range of photon irradiances was available for these measurements.

$$E_q(T) = \Omega \int_0^\infty M_p(\lambda, T) RRPH(\lambda) \tau_{Window}(\lambda) \tau_{filter}(\lambda) d\lambda \tag{7}$$

where:

- Ω = solid angle of the detector FOV, steradians
- $M_p(\lambda, T)$ = Blackbody photon exitance evaluated at temperature, T, $\frac{photons}{s - cm^2 steradian \mu m}$

- $RRPH(\lambda)$ = detector relative spectral Response
- $\tau_{Window}(\lambda)$ = vacuum window transmittance
- $\tau_{filter}(\lambda)$ = filter transmittance
- $E_q(T)$ = signal photon irradiance from a blackbody at temperature T, , $\frac{photons}{s-cm^2}$

4.1.3. Γ Measurement of the Microgrids in the FPA

To characterize Γ of the microgrid polarizers on the FPA, the responsivity was measured as a function of the rotation angle of the Thor Lab polarizer. The Thor Lab WGP is referred to as the state generating polarizer or simply the state generator. Γ of the state generator was measured to be 1:146.[13] This polarizer was mounted on the liquid helium cold shield and could be rotated through 360 in increments of 22.5. The exact orientation of the state generator was not known relative to the orientation of the microgrids. All angular measurements are reported relative to the initial position of the state generator. The responsivity is calculated from the change in FPA output per unit irradiance and knowledge of the detector area and integration time. This method is the preferred methodology for measuring responsivity because it accounts for non-uniformities in the output due to dark current and offsets in the ROIC. During this polarmetric characterization, the measured responsivity values will vary as a function of the rotation angle of the dewar polarizer according to Malus Law:

In the case where the state generator is crossed with the microgrid polarizer, the responsivity of the FPA will be very low and challenging to measure. To overcome this challenge, the responsivity was determined by measuring the FPA output as a function of integration time while operating under high photon irradiance conditions. The responsivity is calculated using Eq. 8, which requires knowledge of the photon irradiance, detector area, ROIC conversion gain (transimpedance), and the dark current.

$$\begin{aligned} Responsivity &= \frac{dV_{Output}}{d(E_q A_{det} \tau_{int})} \\ &= \frac{\left(\frac{dV_{Output}}{d(\tau_{int})} - \frac{C_g I_{Dark}}{q}\right)}{A_{det} E_q} \frac{Volts}{photon} \end{aligned} \tag{8}$$

where:

- dV_{Output} = change in output voltage
- τ_{int} = sensor integration time

- A_{det} = active area of sensor
- I_{Dark} = sensor dark current
- q =electronic charge
- E_q = signal photon irradiance from a blackbody at temperature T, , $\frac{photons}{s-cm^2}$

This measurement technique requires a more thorough knowledge of the FPA characteristics in order to accurately determine the responsivity; however, it also provides a convenient methodology when the polarizers are crossed and the effective FPA responsivity is reduced. The results of measuring the FPA responsivity are shown in Fig.4(a) which plots the measured median responsivity for all 4 pixels in a sub-quad versus the state generator's rotation angle. In addition, a fit to the data using Malus law is provided, which demonstrates that the Micro-Grid polarizer FPA is operating properly. These data also show that when the Thor Lab polarizer and the microgrid polarizer, orientated at 135, are crossed, which occurs at rotation angles of 0 and 180 (recall that angular measurements are relative to the initial position of the state generator) in the data presented in Fig.4(a), the FPA responsivity is approximately 2.3 nV/photon. As described by Γ, this responsivity is approximately a factor of ten lower than compared to the case when the polarizers are aligned. To demonstrate the efficacy of the responsivity measurement, consider the case where the responsivity is measured under nominal FPA operating conditions (τ_{int} = 280 μ sec) when the Thor Lab polarizer and the microgrid polarizer are crossed. This case presents the lowest responsivity condition and to achieve a signal that consumes fifty percent of the ROIC signal swing under nominal operating conditions requires a photon irradiance of over $3x10^{17}$ $photons/sec - cm^2$, a value that is approximately a factor of 30 higher than the FPAs nominal operating irradiance, which is difficult to achieve experimentally. This calculation demonstrates that determining the responsivity by measuring the FPA output as a function of integration time is the more appropriate technique for these measurements.

The Γ(s) determined from these data are summarized in Table 4.1.3 that describes the responsivity when the polarizers are crossed, the responsivity when the polarizers are aligned, and the calculated extinction ratio for the median pixel for each pixel in the subquad. These measurements demonstrate that the lowest measured FPA responsivity, with the polarizers crossed, is approximately 2 nV/photon. The last column is the mean Γ values as determined by the second measurement method.

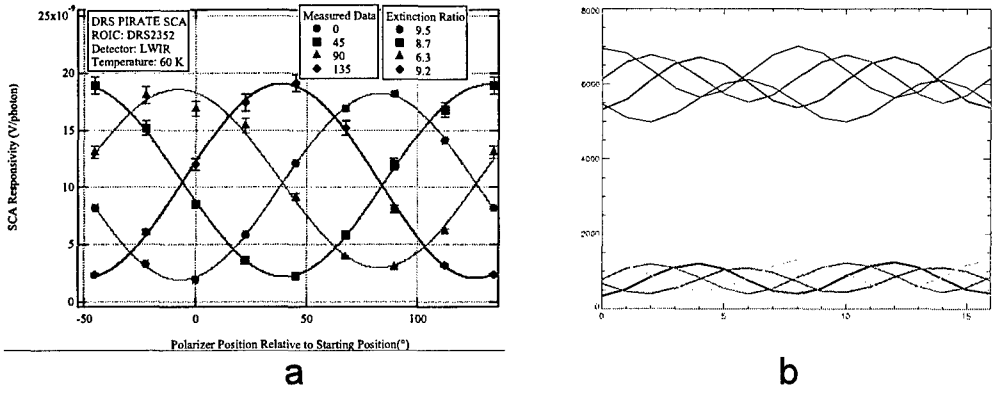

Figure 4. a) Calibration data taken with cold components. (b) Calibration data taken with hot-cold subtraction scheme.

Table 4.1.3. Summary of measured extinction ratios in the microgrid FPA				
microgrid (deg)	Responsivity Crossed (nV/photon)	Responsivity Aligned (nV/photon)	Mean Γ Method 1	Mean Γ Method 2
0	1.9	18.2	9.5	8.2
45	2.2	19.0	8.7	7.4
90	2.9	18.1	6.3	5.8
135	2.1	19.1	9.2	7.6

4.2. Method 2: Differencing Polarized Input

The second method to estimate polarization calibration coefficients is the differencing method where the components of the state generator are at room temperature.[14] The recipe is to take polarized flat-field data at hot and cold blackbody temperatures and then subtract the data and thereby eliminate the common background. Example data for this method is displayed in fig. 4b. The curves at the top of the this plot are from a single sub-quad exposed to a hot (50C) polarized source only. The bottom curves in the plot are from the same pixels after the hot-cold subtraction. The background and offset unique to each pixel has been subtracted which is evident in the tightly clustered curves at the bottom of the plot. Γ results from this method are given in 4.1.3. A brief mathematical description follows.

As with the first method, the second method of measure depends on the oscillation captured by the law of Malus. The recipe to collect data follows that used in the first method except that the state generator was at room temperature and little effort was made to limit background. The polarizer used for the state generator was a 2 inch WGP with

a measured Γ of 200:1. While the subtraction technique should mitigate problems from unwanted signals, we were still susceptible to drifts during the approximate 60 minutes it took to gather up all of the required data.

Straight forward manipulation yeilds the expected radiance at the dectector after the blackbody signal has been polarized and subsequently analyzed. The variables θ and ϕ are used for the polarizer and analyzer angles respectively. Equation 9 is the background subtracted radiance at the detector.

$$S_{0d}(\Delta T, \theta, \phi) = \\ A\Omega \int_\lambda L_{BB}(\Delta T) \left[(q_p + r_p)(q_A + r_A) + (q_p - r_p)(q_A - r_A)\cos(2\theta - 2\phi)\right] d\lambda \tag{9}$$

$L_{BB}(\Delta T)$ represents the radiance difference between hot and cold black-body settings, p subscript indicates the front polarizer and A subscript indicates the microgrid analyzer on the pixel. The $A\Omega$ term accounts for the optical throughput and integration over λ accounts for the spectral bandpass. The resulting units for S_{0d} are $\frac{photons}{sec}$. Eq. 9 is a mathematical expression for the waves shown at the lower portion of the plot in Fig. 4. The rotating polarizer of the state generator makes θ the produces the abscissa in Fig. 4. Note that the finite Γ of the polarizer has been carried through to this point. Backgrounds are subtracted out, but varying detector gain has yet to be addressed. Fourier transforming the signal and subsequently capturing the DC and 2θ coefficients demodulates the data. Basic ratios complete the estimates for Γ and analyzer orientation. Tracing the steps to obtain Eqs. 10 & 11 will reveal that the Γ of the state generator has allowed us to drop its contribution to the result. This assumption accounts for the approximation indicated in these equations.

$$[\Gamma_A]^{-1} \approx \frac{F[L_d(\Delta T)]_{DC} - 2F[L_d(\Delta T)]_{2\theta}}{F[L_d(\Delta T)]_{DC} + 2F[L_d(\Delta T)]_{2\theta}} \approx \frac{r_A}{q_A} \tag{10}$$

$$\phi_A = \frac{1}{2}\tan^{-1}\left(\frac{ImF[L_d(\Delta T)]_{2\theta}}{ReF[L_d(\Delta T)]_{2\theta}}\right) \tag{11}$$

There is still the ever present concern of detector gain. Gain is the proportionality constant that transforms the signal to counts measured by the device and it is assumed to be linear over the range of temperatures used to create the data set. This is an approximation. Consequently there is a balance in this data between separating hot can cold data sets enough to create a signal over the noise and keeping the two temperatures close enough to avoid nonlinear effects from the detector. If the linearity assumption holds up, then detector gain will become a proportional constant attached to all radiance terms which

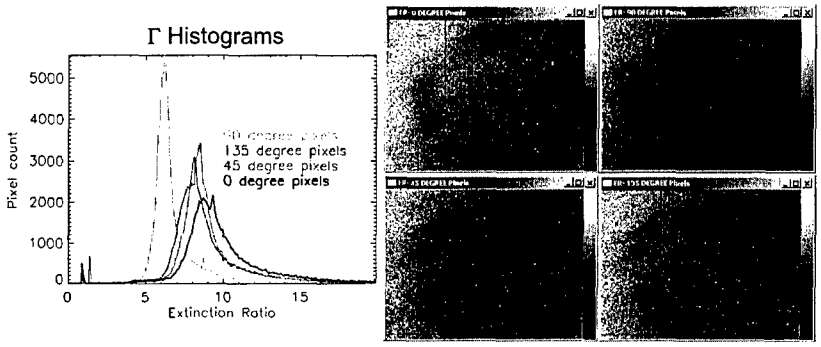

Figure 5. Histograms and spatial display of measured Γ data using method 1

are subsequently divided out by eqs. 10 and 11 making gain benign. We assumed that the linearity assumption was reasonably good in the data presented here but it is certainly an area for further investigation.

The process described was used to estimate the extinction ratio and phase of all pixels in the DRS microgrid HgCdTe array. The table in the previous section summarized the data numerically. Figs. 5 and 6 display histograms of the measured Γ values for measurement method 1 and 2 respectively. Also shown are images created from the measured values which helps to gauge spatial uniformity. In both figures the images show sorted data with: upper left mapping out all of the pixels with horizontal microgrids, upper right being vertically polarized pixels, lower left being 45^o pixels, and lower right being 135^o pixels. The spatial maps suggest the state generator may have had a problem, particularly in method 1, while the data summarized in the last section suggest the estimates in method 2 may be too low.

5. MEASURING PERFORMANCE OF DRM

Because we know that measurements can precipitate as many problems as they attempt to solve, we wish to gauge how much good we have done by applying the calibration to data. Applying the polarimetric correction is straight forward as outlined in Section 3. Gauging the effects can be difficult. Consequently we chose to examine the corrected data in 3 different ways. In all cases we chose to only apply calibration estimates for Γ only and ϕ values we taken as their theoretically ideal values Results summarized are specific to the DRS HgTeCd microgrid which is mounted in a cryogenically cooled camera assembly.

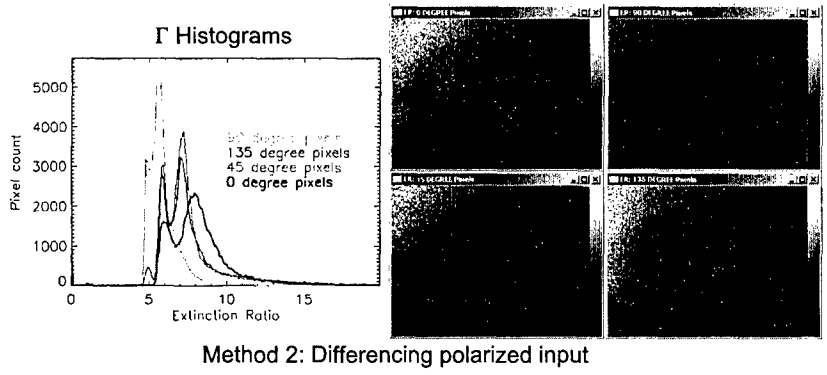

Figure 6. Histograms and spatial display of measured Γ data using method 2

The first analysis is to apply the correction to flat-field, uniformly polarized data. From this type of input, we would expect every sub-quad to estimate the same state of polarization. Creating histograms should illuminate how well the calibration corrects the data. In short, a perfect calibration along with perfect input should produce a delta function histogram. In practice this never happens, but the narrowing and center of the histogram still are excellent indicators of performance. Fig. 7 plots the histograms from flat-field polarized input where for both calibrated and uncalibrated DOLP estimates. Fig. 7a are results from coefficients measured with method 1 while Fig. 7b are results from method 2. The first observation is the shift to higher DOLP values for the average estimate in the calibrated results. This is expected particularly in light of the Γ estimates of Table 4.1.3. In short, low Γ means that the sensor thinks it is measuring unpolarized light when in truth it is polarized light which has leaked through the microgrid. Both calibration attempts accurately correct this mistake. Now examine the width and height of the histograms. Method 1 appears to have narrowed and spiked its histogram which is exactly what we sought. Unfortunately we found this in only one data set used to test the calibration. In all other data sets, the results appeared much closer to those shown in Fig. 7b. This portion of the figure shows results from examining the same test data with the coefficients measured with method 2. This suggests that the response of the sensor is less uniform after calibration, exactly the opposite of the goal. Generally this trend was found in both calibration techniques when many test data where analyzed. It is possible that the fault lies in the input assumed uniform flat-field polarized data. To test this possibility, we tested many input data but the poor trend in histograms remained. This illustrates the difficulty in obtaining a good polarimetric calibration for the purposes of improving image clarity.

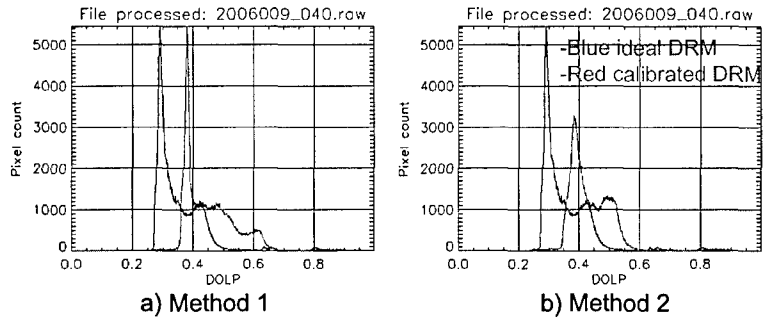

Figure 7. Histograms from flat-field polarized data

A second question to ask when calibrating an array is: which pixels were corrected? This is graphically illustrated in Fig. 8. In this figure, all pixels are plotted on the equatorial plane of the Poincarè sphere refered to here as the Poincarè disk. The horizontal axis plots normalized S_1 values and the vertical axis plots normalized S_2 values. Consequently, radial position indicates a pixel's DOLP value and the angular position indicates the linear polarization orientation. Specifically, the linear orientation is half the angular measure on the Poincarè disk. The disk is then used to sort the data by selecting regions of interest (ROI)s. The FPA plots shown in Fig. 8 are binary maps where black indicates the pixel is not contained in ROI selected on the Poincarè disk and white indicates the pixel is in the ROI. Here a new fact not evident in the histogram arises. That is that the calibration has helped the low spatial frequency of polarimetric estimates but done little for the pixel-to-pixel estimates or high spatial frequencies. Consequently, even with both calibration techniques, only low spatial frequencies are captured. As in Fig. 7, points in red indicate calibrated estimates and blue points are uncalibrated estimates. Our expectation is that the calibrated points would cluster into a very tight group on the disk. Instead the Poincarè disk plots suggest that some well behaved pixels are improved while many others are scattered, exactly the opposite of what we wish. This result was true for coefficients from both methods of calibration.

The third examination of calibration performance is seen in actual images. In short, it is hoped that a calibration will improve image quality. To test this we imaged a heated black sphere located in the laboratory. The sphere is an excellent target since it provides the full range of linear orientations in polarization as well as many levels of DOLP.[15] Further, the slowly varying nature of the signal allows for an ideal object whose polarimetric image might be improved through calibration. Actual DoLP sphere images along with a cross-sectional plots are shown in Fig. 9. Images from uncalibrated data, method 1 and method 2 are shown as indicated. The cross-sectional plots are color coded as indicated by the

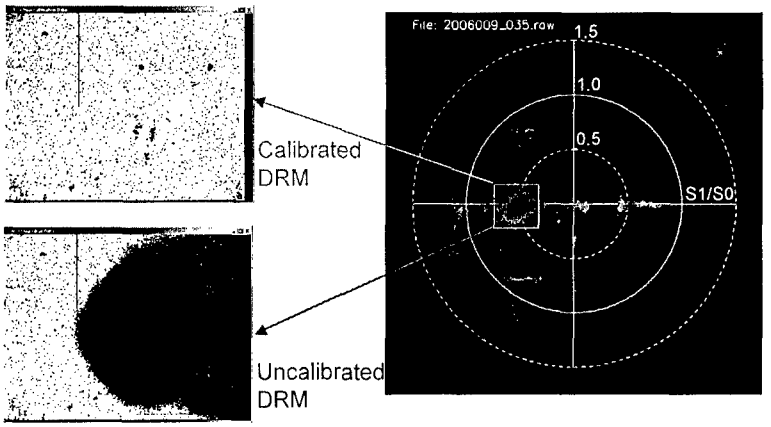

Figure 8. Data sorted on the disk and results plotted back to the imaging array

labels on the images. This look at the data acts to support the conclusions made in the histograms of Fig. 7 as well as the maps shown in Fig. 8. That is, while the net DoLP estimate is boosted, high spatial frequency noise seems to be unaffected.

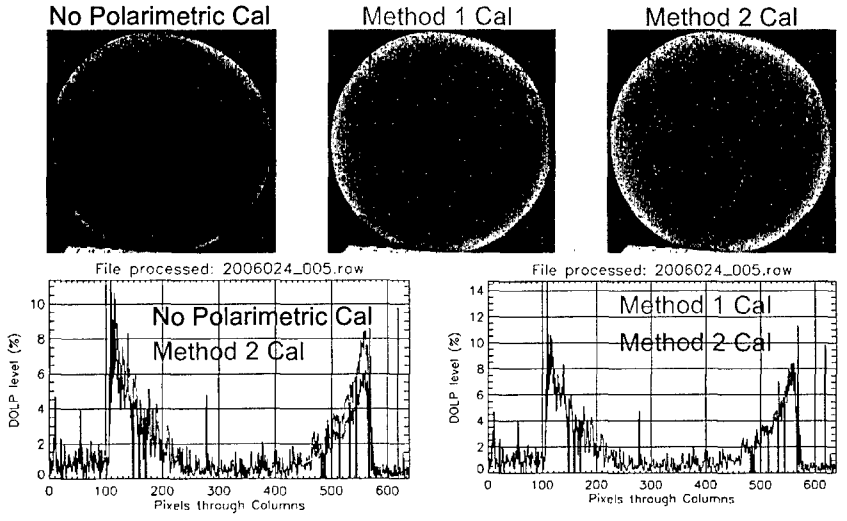

Figure 9. Measuring DoLP from a spherical target with calibrated and uncalibrated data

6. CONCLUSIONS

Applying a polarimetric calibration to an imaging polarimeter might be regarded as an obvious step. The method to apply a calibration has been presented and is reasonably simple to do. While it is recommended to do this calibration on LWIR IP, we acknowledge that the benefits are limited. Specifically, low spatial frequencies are corrected well, and DOP estimates are appropriately boosted, compensating from WGP which appear to be a bit low in ER. On the other hand, the high spatial frequencies, that is the pixel-by-pixel polarization estimate, appear to be nearly unaffected by our polarimetric calibration attempts. This is true for two independent attempts to estimate the FPA polarization coefficients. In fact, in all three analysis of the data, spatial noise in the estimate appear to be worse. This is true for multiple attempts at obtaining noise free calibration coefficients.

7. ACKNOWLEDMENTS

The authors would like to acknowledge Robert Mack of AFRL/SNJT for collaboration on and continued use of the cryogenically cooled camera. J. S. Tyo and J. K. Boger were supported in part by the Air Force Office of Scientific Research under award #FA9550-05-1-0090 and the National Science Foundation under award # 0238309.

REFERENCES

1. L. J. Cheng, M. Hamilton, C. Mahoney, and G. Reyes, "Analysis of aotf hyperspectral imaging," in *Proceedings of SPIE Vol. 2231, Algorithms for Multispectral and Hyperspectral Imagery*, A. Iverson, ed., pp. 158–166, SPIE, (Bellingham, WA), 1994.
2. J. S. Tyo, M. P. Rowe, E. N. Pugh, and N. Engheta, "Target detection in optically scattering media by polarization-difference imaging," *Appl. Opt.* **35**, pp. 1855–1870, 1996.
3. L. B. Wolff and T. E. Boult, "Constraining object features using a polarization reflectance model," *IEEE Trans. Patt. Analysis Machine Intell.* **13**, pp. 635–657, 1991.
4. D. L. Bowers, J. K. Boger, D. Wellems, W. T. Black, S. E. Ortega, B. M. Ratliff, M. P. Fetrow, J. E. Hubbs, and J. S. Tyo, "Evaluation and display of polarimeteric image data using long-wave cooled microgrid focal plane arrays," in *Proc. SPIE vol. 6240: Polarization: Measurement, Analysis, and Remote Sensing VII*, D. H. Goldstein and D. B. Chenault, eds., SPIE, (Bellingham, WA), 2006.
5. J. S. Tyo, E. N. Pugh, and N. Engheta, "Colorimetric representations for use with polarization-difference imaging of objects in scattering media," *J. Opt. Soc. Am. A* **15**, pp. 367–374, 1998.
6. A. G. Andreou and Z. K. Kalayjian, "Polarization imaging: principles and integrated polarimeters,"
7. E. Collett, *Polarized Light, Fundamentals and Applications*, Marcel Dekker, New York, 1992.
8. R. M. A. Azzam and N. M. Bashara, *Ellipsometry and Polarized Light*, North-Holland, New York, 1977.
9. R. A. Chipman, "Polarimetry," in *Handbook of Optics*, M. Bass, ed., **2**, ch. 2, McGraw-Hill, 1995.
10. R. M. A. Azzam, I. M. Elminyawi, and A. M. El-Saba, "General analysis and optimization of the four-detector photopolarimeter," *J. Opt. Soc. Am. A* **5**, pp. 681–689, 1988.

11. R. M. A. Azzam, "Arrangement of four photodetectors for measuring the state of polarization of light," *Opt. Lett.* **10**, pp. 309–311, 1985.
12. B. M. Ratliff, R. Kumar, J. S. Tyo, and M. M. Hayat, "Combatting infrared focal plane array nonuniformity noise in imaging polarimeters," in *Proc. SPIE vol. 5888: Polarization Science and Remote Sensing II*, J. A. Shaw and J. S. Tyo, eds., SPIE, (Bellingham, WA), 2005.
13. J. E. Hubbs, M. E. Gramer, D. Maestas-Jepson, G. A. Dole, M. P. Fetrow, D. L. Bowers, and J. K. Boger, "Measurement of the radiometric and polarization characteristics of a microgrid polarizer infrared focal plane array," in *Proc. SPIE vol. 6295: Infrared Detectors and Focal Plane Arrays VIII*, E. L. Dereniak and R. E. Sampson, eds., SPIE, (Bellingham, WA), 2006.
14. C. M.Persons, M. W. Jones, C. A. Farlow, K. D. Spradley, M. G. Gulley, T. W. Owens, and B. S. Yeske, "Polarimetric calibration by direct measurement of the system mueller matrix," in *2004 Conference on Characterization and Radiometric Calibration for Remote Sensing*, Utah State University Space Dynamics Laboratory, 2004.
15. J. K. Boger, J. S. Tyo, B. M. Ratliff, M. P. Fetrow, W. T. Black, and R. Kumar, ""Modeling precision and acuracy of a LWIR microgrid array imaging polarimeter"," in *Proc. SPIE vol. 5888: Polarization Science and Remote Sensing II*, J. A. Shaw and J. S. Tyo, eds., pp. 227–238, SPIE, 2005.

The Effects of Thermal Equilibrium and Thermal Contrast in Polarimetric Images in the LWIR

J. Scott Tyo
College of Optical Sciences, University of Arizona, Tucson, AZ 85721 USA
tyo@ieee.org

James K. Boger[+], Bradley M. Ratliff, Wiley T. Black, David L. Bowers
Applied Technology Associates, 1300 Britt St. SE, Albuquerque, NM 87123 USA

Matthew P. Fetrow
US Air Force Research Laboratory/VSSS, 3550 Aberdeen SE, Kirtland AFB, NM 87117 USA

Abstract: Long-wave infrared (LWIR) polarimetric signatures provide the potential for day-night detection and identification of objects in remotely sensed imagery. The source of optical energy in the LWIR is usually due to thermal emission from the object in question, which makes the signature dependent primarily on the target and not on the external environment. In this paper we explore the impact of thermal equilibrium and the temperature of (unseen) background objects on LWIR polarimetric signatures. We demonstrate that an object can completely lose its polarization signature when it is in thermal equilibrium with its optical background, even if it has thermal contrast with the objects that appear behind it in the image.

OCIS codes: (000.0000) General.

References and links

1. J. S. Tyo, D. H. Goldstein, D. B. Chenault, and J. A. Shaw, "Review of Passive Imaging Polarimetry for Remote Sensing Applications," Appl. Opt. **45**, 5453 – 5469 (2006).
2. O. Sandus, "A review of emission polarization," Appl. Opt. **4**, 1634–1642 (1965).
3. T. J. Rogne, "Passive detection using polarized components of infrared signatures," in *Proceedings of SPIE vol. 1317: Polarimetry: Radar, infrared visible, ultraviolet and X-ray*, R. A. Chipman and J. W. Morris, eds., pp. 242 – 251 (SPIE, Bellingham, WA, 1990).
4. R. A. Millikan, "A study of the polarization of the light emitted by incandescnet solid and liquid surfaces. I." Phys. Rev. **3**, 81–99 (1895).
5. R. A. Millikan, "A study of the polarization of the light emitted by incandescnet solid and liquid surfaces. II." Phys. Rev. **3**, 177–192 (1895).
6. D. L. Jordan, G. D. Lewis, and E. 'Jakeman, "Emission polarization of roughened glass and aluminum surfaces," Appl. Opt. **35**, 3583 – 3590 (1996).
7. R. M. A. Azzam and N. M. Bashara, *Ellipsometry and Polarized Light* (North-Holland, New York, 1977).
8. S. Chandresekhar, *Radiative Transfer* (Dover, New York, 1960).
9. J. A. Shaw, "Degree of linear polarization in spectral radiances from water-viewing infrared polarimeters," Appl. Opt. **38**, 3157–3165 (1999).
10. J. K.Boger, J. S. Tyo, B. M. Ratliff, M. P. Fetrow, W. Black, and R. Kumar, "Modeling precision and accuracy of a LWIR microgrid array imaging polarimeter," in *Proc. SPIE vol. 5158: Polarization Science and Remote Sensing*, J. A. Shaw and J. S. Tyo, eds., p. 58880U (SPIE, Bellingham, WA, 2005).
11. D. Bowers, J. K. Boger, L. D. Wellens, W. T. Black, S. E. Ortega, B. M. Ratliff, M. P. Fetrow, J. E. Hubbs, and J. S. Tyo, "Evaluation and display of polarimetric image data using long-wave cooled microgrid focal plane

arrays," in *Proc. SPIE vol. 6240: Polarization: Measurement, Analysis, and Remote Sensing VII*, D. H. Goldstein and D. B. Chenault, eds., p. 6240OF (SPIE, Bellingham, WA, 2006).
12. A. G. Andreou and Z. K. Kalayjian, "Polarization imaging: principles and integrated polarimeters," IEEE Sensors Journal **2**, 566 - 576 (2002).
13. B. M. Ratliff, J. K. Boger, M. P. Fetrow, J. S. Tyo, and W. T. Black, "Image processing methods to compensate for IFOV errors in microgrid imaging polarimeters," in *Proc. SPIE vol. 6240: Polarization: Measurement, Analysis, and Remote Sensing VII*, D. H. Goldstein and D. B. Chenault, eds., p. 6240OE (SPIE, Bellingham, WA, 2006).
14. R. A. Chipman, "Polarimetry," in *Handbook of Optics*, M. Bass, ed., vol. 2, chap. 22 (McGraw-Hill, 1995).
15. J. E. Hubbs, M. E. Gramer, D. Maestas-Jepson, G. A. Dole, M. P. Fetrow, D. L. Bowers, J. K. Boger, and E. Atkins, "Measurement of the radiometric and polarization characteristics of a microgrid polarizer infrared focal plane array," in *Proceedings of SPIE vol. and 6295: Infrared Detectors and Focal Plane Arrays VIII*, E. L. Dereniak and R. E. Sampson, eds., p. 62950C (SPIE, Bellingham, WA, 2006).
16. J. K. Boger, J. S. Tyo, B. M. Ratliff, M. P. Fetrow, W. Black, and R. Kumar, "Modeling precision and acuracy of a LWIR microgrid array imaging polarimeter," in *Proc. SPIE vol. 5888: Polarization Science and Remote Sensing II*, J. A. Shaw and J. S. Tyo, eds. (SPIE, Bellingham, WA, 2005). In Press.
17. G. D. Bernard and R. Wehner, "Functional similarities between polarization vision and color vision," Vision Research **17**, 1019–1028 (1977).
18. L. B. Wolff, "Polarization Camera For Computer Vision With A Beam Splitter," J. Opt. Soc. Am. A **11**, 2935–2945 (1994).
19. J. S. Tyo, E. N. Pugh, and N. Engheta, "Colorimetric Representations For Use With Polarization-Difference Imaging Of Objects In Scattering Media," J. Opt. Soc. Am. A **15**, 367–374 (1998).

1. Introduction

Imaging polarimetry has emerged as a powerful tool to aid in the detection and identification of objects in remotely sensed imagery in all regions of the optical spectrum [1]. Polarimetric imagers are usually designed to sense the polarization properties of the reflected polarization signatures, though it is well known that emitted radiation can also be partially polarized [2]. In order to have enough emitted radiation to reliably detect the polarization signatures, it is been necessary to either work with very hot targets or sense in the long-wave infrared (LWIR, $8-12\ \mu$m). There has been interest in LWIR imaging polarimetry dating back more than 20 years [3], with many imaging and non-imaging devices built and tested in the intervening years [1]. The purported advantages of polarimetric sensing in the LWIR include independence from any external source of radiation and invariance of signatures with respect to time-of-day. These advantages are assumed to come from the fact that the source of radiation is thermal emission from objects in the scene.

Emission polarimetry has been thoroughly studied by many authors. Early experiments were done by Millikan [4, 5], and a thorough review is provided by Sandus [2]. The experimental evidence has demonstrated that conservation of energy must be satisfied for the two polarization states independently:

$$\varepsilon_s(\theta)+r_s(\theta) = 1 \quad (1)$$

$$\varepsilon_p(\theta)+r_p(\theta) = 1 \quad (2)$$

where ε is the emissivity and r is the power reflectivity in the $s-$ and $p-$ polarization states and θ is the direction of observation as indicated in fig. 1. Eqn. (1) assumes that the object is isotropic, opaque, that all energy is either reflected or absorbed, and that the absorptivity is equal to the emissivity in each polarization state. Any feature of the object that allows mixing of s- and p-polarization states such as chirality, anisotropy, or severe multiple scattering will force the use of a more exact model. Eqn. (1) further neglects bidirectional reflection, but is approximately accurate for highly emissive targets [6]. The s- and p- reflectivity are calculated using the standard Fresnel reflection coefficients [7] with appropriate complex index of refraction $\tilde{n} = n + ik$ that can effectively take surface roughness into account [2, 6]. If an object is significantly warmer than its background, then the polarization signature is dominated by emis-

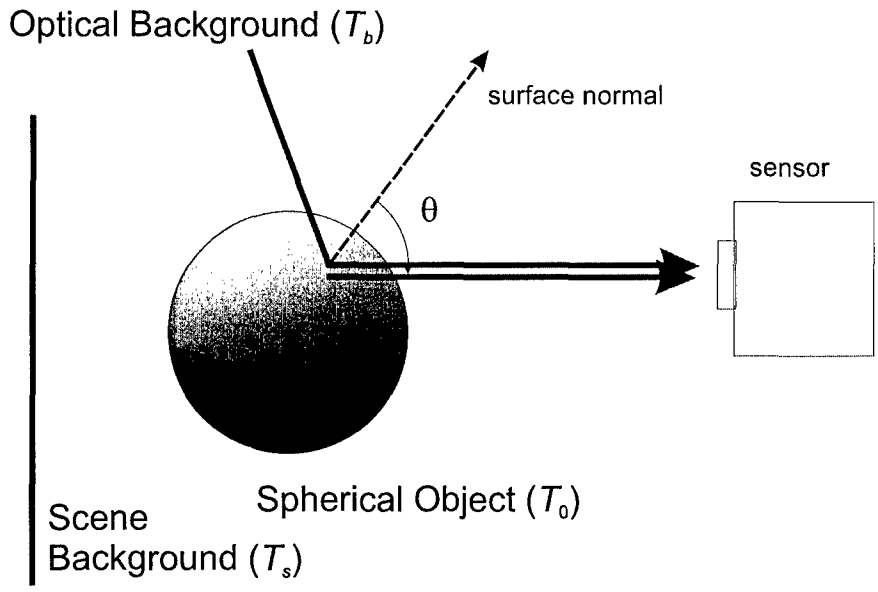

Fig. 1. Geometry and coordinates for LWIR emission/reflection from a spherical object.

sion from the object. When this is the case the polarization signature is independent of time of day, specific object temperature, etc.

Consider the geometry shown in fig. 1. Given (1), and assuming an unpolarized background with emissivity equal to unity and temperature T_b, we have the total s-polarized spectral radiance leaving the object at temperature T_o in direction θ (in [W cm^2 sr μm])

$$L_\lambda^{(s)}(\theta) = P(T_o)\varepsilon_s(\theta) + P(T_b)r_s(\theta) \tag{3}$$

where $P(T)$ is the Planck blackbody radiance curve at temperature T. A similar equation holds for the p-polarized radiance. In (3) we assume that the emissivity and reflectivity are spectrally flat over the wavelength range of interest, which is a reasonable assumption when working in the LWIR. It is important to note that T_b in (3) refers to the optical background, i.e. the object that is in the specular direction with respect to the observer as depicted in fig. 1. The background *does not* refer to the scene background. Strictly speaking, (3) should be replaced by the complete radiative transfer equation [8], but the expression as written is accurate enough for reasonably smooth objects in air.

Using (1) in (3) gives us

$$\begin{aligned} L_\lambda^{(s)}(\theta) &= P(T_o)(1 - r_s(\theta)) + P(T_b)r_s(\theta) \\ &= P(T_o) + r_s(\theta)(P(T_b) - P(T_o)) \end{aligned} \tag{4}$$

for s-polarization and

$$\begin{aligned} L_\lambda^{(p)}(\theta) &= P(T_o)(1 - r_p(\theta)) + P(T_b)r_p(\theta) \\ &= P(T_o) + r_p(\theta)(P(T_b) - P(T_o)) \end{aligned} \tag{5}$$

for p-polarization.

There are three different regimes that exist for exploiting polarimetric signatures as summarized by Rogne [3]. The first is the reflective regime where $T_b >> T_o$. In this case the measured polarization signature is primarily due to reflections from the surface of the object. This is the operating regime for most terrestrial imaging applications in the visible, near infraraed, and short-wave infrared.

The second regime occurs when the object is significantly warmer than the background ($T_o >> T_b$). In this case the surface transmission of thermally emitted radiation is the dominant polarization mechanism. For most outdoor terrestrial imaging applications this condition is met in the LWIR, especially when the cold sky is the optical background [3]. Most LWIR polarimetric sensors are designed to exploit data in this operating regime.

When the object is close in temperature with its optical background. Both the reflection and emission contribute significantly to the total radiance leaving the object in the direction of the observer. In such a case it is possible to completely eliminate the polarization signature *even when there is thermal contrast within the image*. It is generally known that an object in thermal equilibrium with its optical background cannot have a polarization signature. However,the role of the *optical* background and *scene* background as defined in fig. 1 are not widely known. It is clear from (4) and (5) that when $T_o = T_b$, the s and p radiances coming from the object are identical, and there is hence no polarization signature. This condition is usually satisfied in the mid-wave infrared (3-5μm) [9], and might be true whether or not there is thermal contrast between the object and the scene background.

2. Sensor Description and Data Processing

The sensor used to gather the data presented in this paper is a LWIR microgrid polarimeter. The polarimeter contains a 640×480 HgCdTe array bonded to an array of wire grid micropolarizers manufactured by DRS Sensors & Tracking Systems. The camera is sensitive to radiation from $8 - 10$ μm. The details of the polarimeter and its calibration are described in more detail elsewhere [10, 11].

The simplest scheme for estimating the Stokes vector at each point in the FPA uses the expressions

$$\mathbf{S} = \begin{bmatrix} s_0 \\ s_1 \\ s_2 \end{bmatrix} = \begin{bmatrix} L_0 + L_{90} \\ L_0 - L_{90} \\ L_{45} - L_{135} \end{bmatrix} \tag{6}$$

where L_0, L_{45}, L_{90}, and L_{135} are the calibrated radiances measured at the neighboring pixels with linear polarizers at the indicated angles. Eqn. (6) ignores the fact that the four pixels have different instantaneous fields of view (IFOV). This IFOV error will result in polarimetric errors in regions of the image where the underlying image is spatially varying. This is an important effect, but is not treated in detail here. Various calibration and compensation strategies have been discussed elsewhere [12, 13].

The camera was radiometrically calibrated using a 2-point calibration with an unpolarized blackbody source at 15 C and 50 C. The data reduction matrices (DRMs) [14, 11] for the individual superpixels were computed as well. The DRM was determined by experimentally measuring the extinction ratio and orientation angle of the wire grid polarizers on a pixel-by-pixel basis [15]. Dead pixels in the FPA were not replaced.

3. Polarimetric Imagery

The test target used for this study is an emissive graybody sphere shown in a visible photograph in fig. 2. The sphere is a 45-cm hollow brass shell painted with Krylon flat black

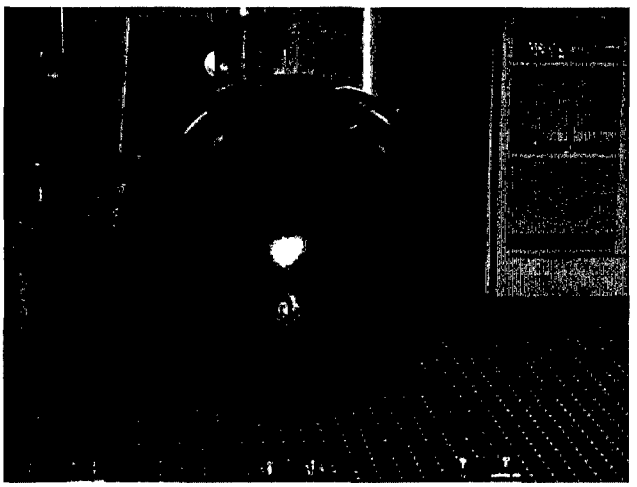

Fig. 2. Visible digital photo of the graybody sphere used as a test target.

paint. Experimental measurements indicate that the effective index of refraction in the LWIR is $\tilde{n} = 1\ 6 + i0\ 1$. The sphere was heated by placing an incandescent lightbulb inside the hollow region and covering the opening with aluminum foil to reduce convective cooling.

For this data collection, the sphere was placed outside our laboratory on a sunny but cool spring day in Albuquerque, NM. The ambient air temperature fluctuated, but was approximately 15 C. The top half of the sphere has the cold sky as a background, with apparent temperature much lower than 0 C [9]. The bottom half of the sphere had the ground as its background. The temperature of the ground was measured to be 28 C using the same thermocouple used to measure the sphere temperature. The sphere was heated to approximately 50 C, and was then allowed to cool until the measured temperature was approximately equal to the ground temperature. Thermocouple measurements indicated that the lower portion of the sphere ranged in temperature from 27 C – 30 C.

We expect the polarization signature of the target to be as follows [2, 16]. For regions of the sphere that have the sky as their optical backgound, the object is primarily emissive, and we expect the polarization to be partially p-polarized. The degree of polarization should be largest near the rim of the sphere where the observation angle is near grazing, and should reduce to zero at the center of the sphere where the observation angle is near normal. The angle of polarization should vary from 0° (with respect to vertical) at the top and bottom of the of the sphere to $\pm 90°$ on the sides.

Fig. 3 shows the reconstructed s_0 and s_1 image of the graybody sphere. We see from fig. 3 that the polarization signature of the object is strongly dependent on the nature of the background. The entire sphere appears to be approximately thermally flat in the s_0 image, but the top half of the sphere, which has $T_b << T_o$ in (4), has a strong polarization signature. The bottom half of the sphere, which has $T_b \approx T_o$ has virtually no polarization signature.

To strengthen this effect, fig. 4a shows the s_0 image of same object imaged under slightly different circumstances. In this case, a human hand with $T \approx 36$ C was placed above the sphere so that the reflected radiation from the hand would reach the imager after reflection from the surface of the sphere. The s_0 image shows that there is a slight increase in apparent temperature due to the reflected radiation from the human hand (as well as the body, which is somewhat less apparent). The reflected radiation from the human hand has little effect on the s_0 image because

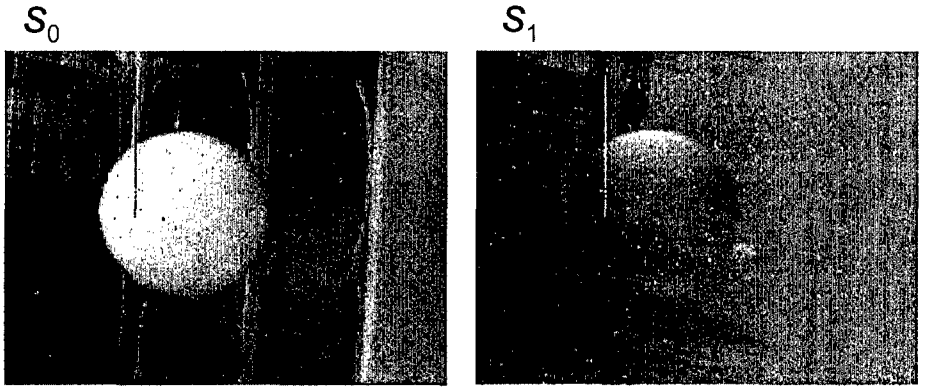

Fig. 3. (a) s_0 image of the heated sphere in the LWIR. (b) s_1 image of the heated sphere in the LWIR.

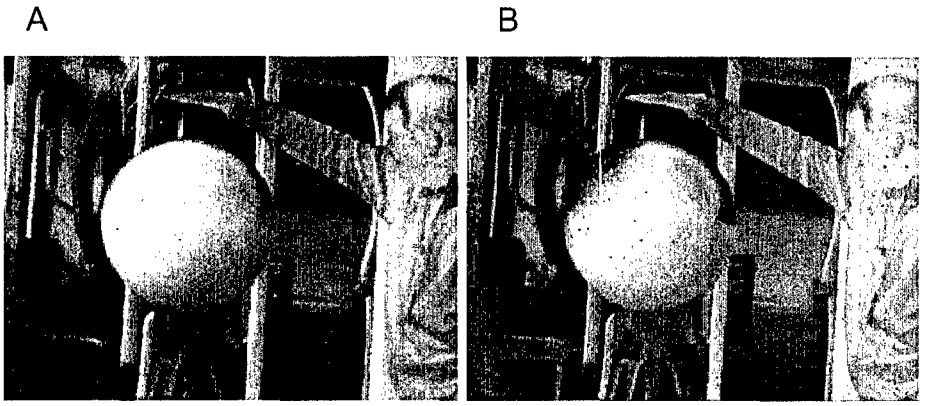

Fig. 4. Polarimetric image of the sphere reflecting radiation from the human hand. (a) s_0 image. (b) Fused polarimetric image using the mapping in (7) – (9).

the object is estimated to have an unpolarized emissivity at normal of 95%.

The situation is much different for the polarizaton imagery. Fig. 4b shows a fused polarimetric image. The Stokes vector data is converted to pseudocolor using an ergonomic color transformation [17, 18, 19]

$$H = 2\psi = \operatorname{atan}\frac{S_2}{S_1} \tag{7}$$

$$S = \mathrm{DoLP} = \frac{\sqrt{{s_1}^2 + {s_2}^2}}{s_0} \tag{8}$$

$$V = s_0 \tag{9}$$

where H, S, and V are the color parameters hue, saturation, and value, ψ is the angle of polarization, and DoLP is the degree of linear polarization. For the imagery in fig. 4 the DoLP is normalized to the maximum measured value of 10% to enhance the saturation of the colors.

4. Discussion and Conclusions

We see from fig. 4b that the presence of the human hand virtually eliminates the polarization signature. Even through the object has low reflectivity ($< 5\%$), the presence of the warm object in the background causes $T_o = T_b$, rendering the DoLP as approximately zero.

LWIR thermal imagery has the significant advantage that thermal contrast is not dependent on the existance of an external source. Any object that is warmer or cooler than the rest of the scene (in terms of apparent temperature, at least) will have thermal contrast.

The polarization properties of emissive objects are more complicated. They depend not only on the object temperature and the temperature of the surrounding objects, but also depend on the temperatures of the optical background objects *that might not even be in the image*. It is intuitive that objects outside the image would be important for both polarized and unpolarized imaging of reflective targets, but the imagery in fig. 3 and fig. 4 shows that the background is just as important for polarized imaging of emissive objects. Even in this case, where the emissivity of the object is close to 1 and almost all of the light reaching the sensor is emitted radiation, the temperature of the background that is seen by the object strongly affects the measured polarization signature.

These results are similar to those presented for spectropolarimetric sensing of the air-water interface. Shaw [9] demonstrated that radiation coming from water in the visible, near IR, and short-wave IR is primarily reflective, while in the LWIR it is primarily emissive. The crossover between these two regimes usually occurs in the mid-wave IR (3-5 μm), and the polarization signature is often quite low there for remote sensing of water.

Acknowledgment

The authors are grateful to David Wellems and Rakesh Kumar for discussions during preparation of this manuscript. Mike Ratliff at Ratliff Metal Spinning Company in Dayton, OH, provided the spherical test target. This work was funded in part by the Air Force Office of Scientific Research, award #FA9550-05-1-0090 and the National Science Foundation under award # 0238309.

[+]Also with the ECE Department, University of New Mexico, Albuquerque, NM, 87131